Variant Selection of Primary - Secondary Extension Twin Pairs in Magnesium: An Analytical Calculation Study

H. Liu[a,1,2], F. X. Lin[b,c, 1,2], P. Liu[d], Y. Yue[e], K. S. Shin[f], L. M. Peng[a], L. Delannay[g], J. F. Nie[d,2], N. Moelans[h]

[a] National Engineering Research Centre of Light Alloy Net Forming and State Key Laboratory of Metal Matrix Composite, Shanghai Jiao Tong University, 200240 Shanghai, PR China
[b] Department of Mechanical Engineering, Technical University of Denmark, DK- 2800 Kgs. Lyngby, Denmark
[c]Department of Physics and Engineering Sciences, Karlstad University, Sweden
[d] DTU Nanolab, Technical University of Denmark, DK-2800 Kgs. Lyngby, Denmark
[e] Department of Materials Science and Engineering, Monash University, Victoria 3800, Australia
[f] Department of Materials Science and Engineering, Seoul National University, 1 Gwannak-ro, Gwannak-gu, Seoul 08826, Republic of Korea
[g]Institute of Mechanics, Materials and Civil Engineering. Université catholique de Louvain, Avenue Georges Lemaître 4-6, Louvain-la-Neuve, Belgium
[h]Department of Materials Engineering, KU Leuven, Kasteelpark Arenberg 44 B, Leuven, Belgium

Abstract

Twining is an important deformation mode in magnesium. In a deformed magnesium sample, an extension twin crystal, i.e., $\{10\bar{1}2\}$ twin, can form inside a $\{10\bar{1}2\}$ primary twin, which is named $\{10\bar{1}2\}$–$\{10\bar{1}2\}$ secondary twin. These secondary twins often appear at the intersection of two primary twins, and form primary–secondary twin pairs. Experimental observations show that the most frequently observed primary–secondary twin pairs have a unique misorientation, i.e., twin variant selection exists. Such variant selection of the primary-secondary twin pairs is studied in this work. The crystallographic analysis reveals that the twin planes of the primary and secondary twins that form a twin pair have coincident intersection lines with the boundary where the twin pair adjoins. An analytical calculation method based on Eshelby's inclusion theory is developed, and the calculation results show that only for this unique misorientation, the stress fields concentrated at the rims of the primary and the secondary twins are mutually favoured. The analysis is further extended to the incoming–outgoing twin pairs across ordinary grain boundaries, and compared with the commonly used geometrical compatibility factor *m'*. It is found that *m'* only gives good prediction for twin transmission when the shear stress component on the twin plane along the twin shear direction of the incoming twin is the major contributor to the resolved shear stress of the outgoing twin. When other stress components play a dominant role, *m'* becomes ineffective in prediction, which is the case for the primary-secondary twin pairs.

Keywords: Secondary twin, variant selection, Eshelby's inclusion theory, twin transmission, twin-twin interaction

---

[1] These authors contribute equally.
[2] Corresponding Authors.
Email address: hong.liu@sjtu.edu.cn, linfx.cn@gmail.com, jianfeng.nie@monash.edu

1. Introduction

As one of the lightest structural metallic materials, magnesium (Mg) alloys have attracted great research interests in aerospace and automobile fields [1–3]. However, limited ductility and strong mechanical anisotropy pose a bottleneck for wider usage of Mg alloys. Compared with metallic materials with a cubic structure such as Al and Cu alloys, Mg alloys have fewer slip systems so that deformation twinning becomes an important deformation mode. Better understanding of deformation twinning is crucial for further improvement of formability and mechanical properties of Mg alloys since deformation twinning influences both ductility and mechanical anisotropy, especially for wrought Mg alloys. At room temperature, extension twin of the $\{10\bar{1}2\}\langle 10\bar{1}1\rangle$ twining system is frequently observed, where $\{10\bar{1}2\}$ is the twin plane and $\langle 10\bar{1}1\rangle$ is the twin shear direction [1–11]. When a $\{10\bar{1}2\}$ twin forms inside a $\{10\bar{1}2\}$ primary twin, it is termed $\{10\bar{1}2\}$–$\{10\bar{1}2\}$ secondary twin or double twin [12–24]. Secondary twins were reported in pure Mg and its alloys under various loading conditions [12–22]. Some $\{10\bar{1}2\}$–$\{10\bar{1}2\}$ secondary twins were observed after uniaxial plastic deformation [16, 21]. They were also frequently observed in samples that had been sequntially compressed from two different directions [17] or cyclically deformed [25]. The $\{10\bar{1}2\}$–$\{10\bar{1}2\}$ secondary twins are effective in refining microstructure, which is beneficial to strength enhancement [26]. However, they are also closely related to crack initiation and propagation [25].

The first observation of the $\{10\bar{1}2\}$–$\{10\bar{1}2\}$ secondary twins was reported by Robert and Partridge [12] in a pure Mg single crystal that has been deformed by four-point bending. They reported that the $\{10\bar{1}2\}$–$\{10\bar{1}2\}$ secondary twin is connected to the primary $\{10\bar{1}2\}$ twin, composing an IPT–RPT–ST configuration, as illustrated in Fig. 1, where RPT is the recipient primary twin within which the secondary twin (ST) forms, and the IPT is the intersecting primary twin that connects the ST at the boundary of the RPT. In this IPT–RPT–ST configuration, the IPT and ST form an adjoining twin pair. Robert and Partridge [12] found that the twin planes of the IPT and the ST intersect that of the RPT at the same line, i.e., the twin planes of the IPT, ST and RPT have a common intersection line, which is $[\bar{2}\bar{2}43]$ of the Mg matrix. Moreover, the twin shear directions of the IPT and the ST both have an angle of 22.83° with the intersection line (Fig. 1, $\alpha_{IPT} = \alpha_{ST} = 22.83°$). A few more examples of such configuration were observed in compressed, rolled and extruded Mg-alloy samples reported by Bian *et al.* [13] and Jager *et al.* [15]. In these studies, the secondary twin forms a pair with an IPT, i.e., an IPT−ST twin pair, although this arrangement of the IPT and ST twins was not mentioned explicitly by the authors. More recently, Xin *et al.* [21] reported that IPT–ST twin pairs were frequently observed in a coarse grained polycrystalline AZ31 (Mg–3wt.%Al–1wt.%Zn) thick plate that has been hot rolled with a strong basal texture. The sample was plastically deformed under uniaxial tension along the normal direction (ND) of the thick plate. Among the 34 IPT–ST twin pairs they examined, 28 have a unique misorientation of $49.7^{o}\langle\bar{9}\ 0\ 9\ \bar{4}\rangle$ between the IPT and the ST. More IPT–ST twin pairs were found by Shi *et al.* [22] in an AZ31 rolled plate under sequential compression along the rolling direction (RD) and the transverse direction (TD). They found that the majority of IPT–ST pairs (66 out of 103) had a misorientation similar to that reported by Xin *et al.* [21]. This unique misorientation indicates that there is variant selection for IPT and ST in an IPT–ST pair. The study of variant selection in an IPT–ST pair might be related to two important issues. The first related issue is twin transmission [27–31]. The IPT–ST twin pair might indeed be the result of a special twin transmission event that occurs across a twin boundary. Twin transmission is an important process for nucleation of new twins in neighbouring grains [32]. The other related issue is the twin-twin interaction [33–35]. The IPT and RPT form a twin-twin junction, and the IPT–RPT–ST configuration corresponds to a special twin-twin interaction where IPT "apparently goes across" RPT [14]. It is then needed to understand which variants of the primary and secondary twins may have such interaction. Although IPT–ST twin pairs were reported by many researchers, the variant

selection has not been well explained yet.

The geometrical compatibility factor, *m′*, has been used to explain why a ST tends to form a twin pair with an IPT, and why there is a preferential misorientation between the ST and the IPT [21, 22, 24]. The geometrical compatibility factor *m′* is expressed by $\cos\varphi \cdot \cos\lambda$, where φ and λ are angles between twin shear and twin plane normal directions of the two twin crystals [36]. A twin pair is considered to be favoured to form when *m′* between the two twins in the pair is close to 1. The factor *m′* provides a reasonable prediction on the formation and variant selection of twin pairs across grain boundaries [17, 21–22, 36–40]. However, Shi *et al.* [22, 24] found that *m′* is negative for the majority of their observed IPT–ST twin pairs, and thus the formation of the IPT–ST twin pairs cannot be explained by *m′*.

The Schmid factor has also been used to judge whether a twin variant is favoured to form under an applied external stress. When the Schmid factor is close to 0.5, the twin variant is favoured to form [41–43]. Jain *et al.* [16] reported two ST crystals in a casting Mg alloy AZ80 (Mg−8Al−0.5wt.%Zn) with a random texture, which were compressed to a strain of 0.08 at 77K. They found that the observed secondary twin in one example had a Schmid factor of 0.4, which is the highest among all possible secondary twin variants, but the observed secondary twin in the other example had a negative Schmid factor. Furthermore, the Schmid factors for all ST crystals in 34 IPT–ST twin pairs reported by Xin *et al.* [21] were negative. Thus, the formation of ST, and that of the IPT–ST pair with a preferential misorientation, should be influenced predominantly by a local stress that includes the stress at the rims of the IPT and ST in a twin pair [29], and the back-stress inside the RPT [24]. However, a detailed stress analysis for the IPT–ST pair has not been performed yet.

The local stress can be calculated by full-field modelling approaches such as elasto-visco-plastic fast Fourier transform simulations, finite element methods and phase-field approach [35, 44–55]. The local stress can also be analytically calculated based on Eshelby's inclusion theory [56]. This method was already used to calculate the elastic strain energy and the stress field inside ellipsoidal twin crystals [24, 57–59]. A well-known difficulty in Eshelby's inclusion problem is to determine the exterior elastic field, i.e., the stress field outside an inclusion [60], as the form of the Eshelby tensor is no longer constant, and becomes much more complicated. Mura [61–62] derived the Eshelby tensor outside ellipsoidal inclusions in terms of the harmonic and bi-harmonic potentials of the inclusion. A simpler and more compact expression was derived by Ju and Sun [63]. More recently, based on Ju and Sun's derivation [63], a formula to calculate the external stress field of an elliptic cylindrical inclusion was derived [64–65]. Eshelby's inclusion model and the related tensor for the external field were used in composite materials [66], concrete [67] and geophysical sciences [68], but rarely applied to deformation twinning.

In this work, we apply Eshelby's inclusion theory to calculate the stress fields both inside and outside an ellipsoidal twin crystal. This is a reasonable assumption considering the lenticular shape of the $\{10\bar{1}2\}$ deformartion twins [69–70] in plastically deformed Mg. Furthermore, phase field simulations show that an ellipsoidal shape of a twin crystal is favoured in order to minimise both elastic strain energy and interfacial energy [54]. The results obtained are used to study how the stress field of one twin crystal (IPT or ST) selects the variant of the other twin crystal in an IPT–ST twin pair. This analytical study is then extended to the incoming–outgoing twin pairs across ordinary grain boundaries, and the calculation results are compared with corresponding *m′* values, in order to reveal the physics behind *m′* and to discuss the applicable range of *m′*. Compared with numerical approaches, the analytical approach is highly efficient and does not require large computational storage. Moreover, such approach can be extended to determine the elastic fields, including the displacement, stress, and stain fields, both inside and outside an ellipsoidal inclusion such as twin crystal, dislocation loop, void, martensite plate and precipitate.

In the following, the crystallographic analyses of primary and secondary twin variants, and

different types of IPT–ST pairs are given in Section 2. The experimental observations on the variant selection in IPT–ST pairs in a plastically deformed polycrystalline AZ31 sample and a single crystal pure Mg sample are provided in Section 3. The influence of local stress fields on the variant selection of the IPT–ST pairs is examined by analytical calculations in Section 4. All findings are discussed in Section 5 and summarised in Section 6.

2. Crystallographic analysis

Each deformation twin variant forms via a homogeneous simple shear of the matrix, and the invariant plane of this shear is called the twin plane. Fig. 2a shows one example in which the twin plane is $(10\bar{1}2)$ (green colour) and the twin shear direction $[\bar{1}011]$ is marked by $\boldsymbol{s^1}$. If expressed in the $x_0y_0z_0$ coordinate system (Fig. 2a) where the shear direction and the normal direction of the twin plane are set as x_0 and z_0 directions, respectively, and the corresponding strain-free transformation strain tensor (SFTS) is:

$$\boldsymbol{\varepsilon^0} = \begin{pmatrix} 0 & 0 & -\gamma^0/2 \\ 0 & 0 & 0 \\ -\gamma^0/2 & 0 & 0 \end{pmatrix}, \tag{1}$$

where γ^0 is the magnitude of the twin shear and can be expressed as:

$$\gamma^0 = -\frac{\sqrt{3}a}{3c}\left[\left(\frac{c}{a}\right)^2 - 3\right] , \tag{2}$$

where a and c are lattice parameters of Mg and γ^0 = 0.13 for $\{10\bar{1}2\}$ twin. This strain allows us to adopt a small strain formalism, considering that a finite strain formalism would be a little more accurate but it would have no influence on the variant selection issue.

There are 6 orientation variants of $\{10\bar{1}2\}$ twin crystals and they are numbered Vi (i = 1– 6) in this work. The twinning systems and the orientations of these twin variants are shown in Table 1. The SFTS of all the 6 variants, $\boldsymbol{\varepsilon^i}$ (i = 1 – 6), are expressed in the *XYZ* coordinate system where *X*, *Y* and *Z* are parallel to $[10\bar{1}0]$, $[\bar{1}2\bar{1}0]$ and [0001] of the Mg matrix, respectively. The first one of the six SFTSs, i.e., ε_{ij}^1, is:

$$\varepsilon_{ij}^1 = \frac{s_i^1 n_j^1 + s_j^1 n_i^1}{2} = R_{ik}^1 R_{jl}^1 \varepsilon_{kl}^0 , \tag{3}$$

where $\boldsymbol{s^1}$ is a vector of magnitude γ^0 aligned with the shear direction, $\boldsymbol{n^1}$ is the unit twin plane normal, and $\boldsymbol{R^1}$ is the rotation matrix of the variant V1 from the $x_0y_0z_0$ coordinate system to *XYZ* coordinate system. The strain tensors of the other twin variants can be obtained by symmetry operations.

When a primary twin crystal Vi experiences a simple shear with a magnitude of s^0 again, a secondary twin crystal may form. The secondary twin variant formed in Vi is denoted Vij (j = 1 – 6). To show the orientation of V1 and V1j, the (0002) pole figure of V1 and V1j is given in Table 1. One example is shown schematically in Fig. 2b, in which the lattice of Mg transforms to that of the primary twin variant V1 (marked by M → PT) via a simple shear $\boldsymbol{s^1}$, and then to the secondary twin variant V14 (marked by PT → ST) via another simple shear $\boldsymbol{s^{14}}$. The calculation of the strain tensor $\boldsymbol{\varepsilon^{ij}}$ describing the transformation from Vi to Vij is similar to $\boldsymbol{\varepsilon^i}$. The components of $\boldsymbol{\varepsilon^1}$ and $\boldsymbol{\varepsilon^{1j}}$, as well as the twin shear and twin plane normal directions of V1 and V1j, are listed in Table 2. Note that if $i = j$, detwinning occurs so that the lattice of Vi will transfer back to that of the Mg matrix because $\boldsymbol{\varepsilon^{ii}} = -\boldsymbol{\varepsilon^i}$. This is also clear from the (0002) pole figure given in Table 1, which shows that the [0001]

direction of V11 is superposed to that of the matrix. Thus, variant V*ii* is equivalent to the matrix and will not be discussed further. There are thus 30 secondary twin variants (V*ij*, $i = 1-6$, $j = 1-6$, $i \neq j$) in total.

Any 2 out of 6 primary variants may interact with each other to form an IPT–RPT intersection. These intersections can be classified into 3 crystallographically different types (Figs. 3a−3c). If RPT is fixed to V1, then examples of these 3 types IPT–RPT intersection are V2–V1 (Type I, Fig. 3a), V3–V1 (Type II, Fig. 3b) and V4–V1 (Type III, Fig. 3c). The intersection lines between the twin planes of V2 and V1, V3 and V1, and V4 and V1 are $[4\bar{2}\bar{2}\bar{3}]$, $[\bar{2}201]$, and $[1\bar{2}10]$ of the matrix, respectively. The misorientations between IPT and RPT in Type I, II and III intersections are $60.0^{o}\langle\overline{12}\ 12\ 0\ 1\rangle$, $60.4^{o}\langle\bar{7}\ 8\ \bar{1}\ 0\rangle$ and $7.4^{o}\langle\bar{2}\ 1\ 1\ 0\rangle$, respectively. These are also listed in Table 3.

For each of the three types of IPT–RPT intersections, the twin plane of only one ST variant intersects those of IPT and RPT at a common line, which is reflected by the stereographic projections in Figs. 3d–3f. For example, for V2–V1 intersection (Type I), only the twin plane of V12 intersects the twin planes of V2 and V1 at a common line, which is represented by the point P_1 in Fig. 3d. Therefore, there are three possible IPT–RPT–ST configurations, in which the twin planes of IPT, RPT and ST share the same intersection line. These configurations are V2–V1–V12 (Type I, Fig. 3d), V3–V1–V13 (Type II, Fig. 3e) and V4–V1–V14 (Type III, Fig. 3f). The misorientations and compatibility factors, *m'*, between IPT–ST pairs in these three configurations are listed in Table 3. It is worth mentioning that the *m'* values between IPT and ST in all three configurations are negative. For each type of the configuration, the angles between the common intersection line and the shear direction of IPT/ ST, i.e., α_{IPT} and α_{ST} shown in Fig. 1, are calculated according to Eq. 4:

$$\alpha_t = \arccos\left|\frac{\boldsymbol{s_t}}{s^0}\cdot(\boldsymbol{n_{IPT}}\times\boldsymbol{n_{ST}})\right|, \qquad (t = \text{IPT or ST}) \tag{4}$$

where $\boldsymbol{n_{IPT}}$ and $\boldsymbol{n_{ST}}$ represent the twin plane normal directions of IPT and ST, respectively, and $\boldsymbol{s_t}$ represents the twin shear of the twin crystal *p*. The values of α_{IPT} and α_{ST} for each type of IPT–ST pair are also listed in Table 3.

3. Experimental observations of variant selection of IPT–ST pairs in deformed Mg samples

To investigate which type of IPT–ST pairs forms most frequently in plastically deformed samples and why, two types of samples were investigated. The first was an AZ31 polycrystalline sample with a strong basal texture. This sample was plastically deformed by uniaxial tension with the tensile axis parallel to the basal poles of most grains. This initial texture ensures that different twin variants form inside the same grain, so that twin-twin junctions and IPT–ST pairs may form. For this sample, the focus of the analysis is on the crystallographic features of IPT–ST pairs. The second sample was a pure Mg single crystal compressed sequentially along two different directions to activate more IPT–ST pairs. By characterizing the microstructures ex-situ, the formation and evolution of IPT–ST pairs as a function of the external strain was investigated. Since these two samples were deformed with different applied stresses, it further allows a discussion of the relationship between IPT–ST variant selection and the applied stresses.

3.1 Experimental methods

Two types of deformed samples were prepared. For the first type, the material was a commercially available AZ31 alloy (Mg–3wt.%Al–1wt.%Zn) hot rolled plate with a strong basal texture, where the basal poles of most grains were aligned parallel to the normal direction (ND) of

the as-received plate. A dog-bone-shaped tensile sample was cut from the plate with the tensile direction parallel to the ND. The gauge section was 25 mm long, 10 mm wide and 2 mm thick. The tensile tests were conducted at room temperature to a true strain of 0.04 with a strain rate of 10^{-4} s^{-1}. After unloading, the microstructure of the cross-section of the sample was characterized using electron backscatter diffraction (EBSD) with a step size of 2 μm. For the second one, a single crystal of pure Mg having a cuboid shape with dimensions of 4 mm (length) × 4 mm (width) × 6 mm (height) was prepared for compression test. The length (*X*), width (*Y*) and height (*Z*) directions of the cuboid sample are approximately parallel to the $[10\bar{1}0]$, $[\bar{1}2\bar{1}0]$ and $[0001]$ directions of Mg, respectively. Uniaxial compression tests were performed using a screw-driven Instron 5982 machine, at a constant strain rate of $1 \times 10^{-3}s^{-1}$. The single crystal was first compressed along the *X* direction to a true strain of 0.075, and then compressed along the *Y* direction progressively to a true strain of 0.035. Microstructural features in the compressed sample were characterized by EBSD using a JEOL 7001 FEG SEM machine equipped with an Aztec analysis system. The EBSD sample was prepared by electropolishing using Lectropol-5 electrolytic polishing machine, in a solution containing 20 vol% nitric acid and 80 vol% methanol, at a temperature of $-5℃$ and a voltage of 3V. The step size used for EBSD was 1.2 μm. The EBSD data were processed using the open-source crystallographic toolbox MTEX [71].

3.2 IPT–ST pairs in a deformed AZ31 polycrystalline sample

The microstructure of the plastically deformed AZ31 is shown in Fig. 4a. It contains a large grain with a size of ~ 400 μm and several small grains with sizes less than 100 μm. Different variants of $\{10\bar{1}2\}$ twin crystals can be observed in the big grain. These twin crystals often intersect with each other, forming twin–twin intersections. The $\{10\bar{1}2\}$–$\{10\bar{1}2\}$ secondary twins are observed at some intersections. Most of these secondary twins are connected with primary twin crystals, and form IPT–RPT–ST configurations. In this sample, 12 examples of the IPT–RPT–ST configurations are identified, and typical examples are represented in regions numbered 1–5 in Fig. 4a.

In each region, all IPT–RPT–ST examples belong to the same configuration. Both IPT and RPT crystals have relatively high Schmid factors (close to 0.5, see Table 4), implying that they are favoured to form spontaneously under the applied stress. In contrast, all ST crystals have *negative* Schmid factors, which means that the formation of these ST is not favoured by the applied stress. Furthermore, values of the geometrical compatibility factor *m'* between IPT and ST in all IPT–RPT–ST examples are also *negative* (Table 4). Thus, the appearance of these IPT–ST pairs cannot be explained by *m'* or Schmid factor.

The twin crystals in all the identified IPT–ST pairs have certain specific orientation relationships. For example, examination of local regions 1 and 2 in Fig. 4a, which are enlarged in Fig. 4b, reveals that the three ST crystals embedded in the same RPT belong to two variants, ST*a* and ST*b*. The IPT crystals connecting ST*a* and ST*b* also belong to two variants, which are IPT*a* and IPT*b*, respectively. The RPT and examples of IPT*a*, ST*a*, IPT*b* and ST*b* are labelled in Fig. 4b. In both IPT*a*–ST*a* and IPT*b*–ST*b* pairs, the IPT and ST crystals have a misorientation of $49.6^{o}\langle\bar{9}\ 9\ 0\ 4\rangle$, and the IPT and RPT have a misorientation of $60.0^{o}\langle\overline{12}\ 12\ 0\ 1\rangle$ (Figs. 4c and 4e). These misorientations between IPT and ST, and between IPT and RPT, are the same in all the observed IPT–ST pairs in the sample.

In each IPT–ST pair, the twin planes of IPT, RPT and ST are found to intersect at a common line. This finding is illustrated by two example pairs, IPT*a*–ST*a* and IPT*b*–ST*b* in Fig. 4b. As can be seen from the stereological projections (Fig. 4d for IPT*a*–ST*a* pair and Fig. 4f for IPT*b*–ST*b* pair), for each pair, the three curves representing the twin planes of IPT, RPT and RT intersect with each other at the same point *P*, indicating that the three twin planes intersect at a common line. By examining the IPT/ST, and IPT/RPT misorientations, as well as the intersection of the twin planes of IPT, ST and

RPT, it is found that all the IPT–ST pairs in the sample are Type I, as defined in Section 2.

3.3 IPT–ST pairs in deformed single crystal of pure Mg

Figs. 5a–5d show the progressive change of the microstructure during plastic deformation. After compression along the *X* direction to a true strain of 0.075, the majority part of the initial crystal has been transformed to twin crystals, which is shown in Fig. 5a. After changing the strain path, and compressing along the *Y* direction to a true strain of 0.014, a few secondary twins appear inside some of the primary twins. These secondary twins are thin lamellae and coloured in green in Fig. 5b. Some of the secondary twins are connected with thin primary twins that form during compression along the *Y* direction, forming IPT–ST pairs. One typical example (marked by the rectangle in Fig. 5b) is enlarged and the IPT, RPT and ST for this example are marked in Fig. 5c. The RPT, IPT and ST in this example belong to V1, V2 and V12, respectively. Thus, this IPT–ST pair is a Type I pair.

When the compression strain along the *Y* direction is increased to a true strain of 0.035 (Fig. 5d), the volume fraction of secondary twins is significantly increased. Compared with Fig. 5b, both IPTs and STs become thicker. Most of these secondary twin crystals are connected with primary twins embedded in the residual matrix, forming IPT–ST pairs. There are approximately 110 IPT–ST pairs. The primary twin variants V1, V2 and V6, and the secondary twin variants V12 and V16 in Fig. 5d are filled by different colours in Fig. 5e, according to the labels shown on the right of the Fig. 5e. The most frequently observed IPT–ST pairs are V2–V12 (~95) that belong to Type I. In addition, around 10 V6–V16 pairs are observed, which also belong to Type I.

When compressed along the *Y* direction, Schmid factors of V2 and V12 are 0.43 and 0.36, respectively. Both are the highest among all the primary and secondary twins (Table 5). Thus, the formation of these two variants is favoured by the applied stress. Schmid factors of V6 and V16 are smaller than those of V2 and V12, respectively. It is worth noting that, according to Table 5, V5 and V15 have higher Schmid factors than V6 and V16, and the V5–V15 pair in the V5–V1–V15 configuration (Type 2) also fulfils the condition that the twin planes of IPT, RPT and ST intersect at a common line. However, the V5–V1–V15 configuration is not observed in the sample.

The experimental results show that most of the IPT–ST pairs in the deformed polycrystalline AZ31 sample (12 out of 12) and single crystal pure Mg sample (~105 out of 110) are Type I, which is also the most frequently observed type in previously reported samples. For example, according to the reported misorientations between IPT and ST, as well as IPT and RPT, the majority of IPT–ST pairs in polycrystalline AZ31 samples, deformed under uniaxial tension (28 out of 34 [21]) or under compression (66 out of 110 [22]), are Type I. The IPT–ST pair reported by Roberts and Partridge in a bent pure Mg sample [12] also belongs to Type I by checking the direction of the intersection line between the twin planes of IPT and ST, and the values of α_{IPT} and $\alpha_{ST.}$ The preferential appearance of Type I IPT–ST pair seems to be independent of the loading conditions, and sometimes the IPT and (or) ST variants in this type of pair do not correspond to the highest Schmid factors among all primary and secondary twin variants. Thus, the local stress field at twin–twin intersections have to be considered. This local stress field includes three types of stresses: (*a*) the stress concentrated at the tips of IPT and ST (Note that in 3D, the twin tip is the rim around a twin crystal), (*b*) the back-stress inside RPT, and (*c*) the applied stress at twin–twin intersections.

4. Analytical calculation of the influence of local stress fields on the variant selection of IPT–ST pairs

4.1 Calculation method

One of the straightforward methods to judge whether an arbitrary pre-existing stress field favours the formation of a twin crystal belonging to the *p*th variant (*p* = *i* for primary twin and *p* = *ij* for secondary twin; both *i* and *j* = 1–6 and *i* ≠ *j*) is to calculate the interaction energy between the pre-existing stress field, $\boldsymbol{\sigma}$, and the SFTS of the twin crystal, $\boldsymbol{\varepsilon}^{\mathbf{p}}$ [72–73]:

$$e^{\mathrm{int}} = -\sigma_{mn}(\boldsymbol{r})\varepsilon^{\mathrm{p}}_{mn}. \tag{5}$$

The form of $\boldsymbol{\varepsilon}^{\mathbf{p}}$ was given in Eq. 3. At a certain position $\boldsymbol{r}$, the negative value of e^{int} indicates that the elastic strain energy generated by the stress field can be relaxed by the formation of the twin crystal, i.e., the formation of the twin crystal is energetically favoured. As e^{int} is a scalar, the value of e^{int} does not change when the coordinate system changes.

If $\boldsymbol{\sigma}$ represents the stress field of an isolated twin crystal belonging to the *q*th variant in an infinite space, it can be calculated based on Eshelby's inclusion theory [60–63, 74]:

$$\sigma^{\mathrm{out}}_{ij}(\boldsymbol{r},\mathrm{q}) = C_{ijkl}S_{klmn}(\boldsymbol{r})\varepsilon^{\mathrm{q}}_{mn} \quad , \tag{6a}$$

$$\sigma^{\mathrm{in}}_{ij}(\mathrm{q}) = C_{ijkl}\left(S^{0}_{klmn}\varepsilon^{\mathrm{q}}_{mn} - \varepsilon^{\mathrm{q}}_{kl}\right) \ . \tag{6b}$$

where $\sigma^{\mathrm{out}}_{ij}$ and $\sigma^{\mathrm{in}}_{ij}$ are the stress fields outside and inside the twin crystal, respectively. C_{ijkl} is the elastic tensor, which is assumed to be isotropic for both twin crystal and Mg matrix in this work. This is reasonable since the elastic anisotropy of Mg is low and C_{ijkl} is close to be isotropic [24, 75]. Thus, C_{ijkl} is expressed with two parameters, the Young's modulus E (49.5210 GPa) and Poisson's ratio v_0 (0.2812):

$$C_{ijkl} = \frac{Ev_0}{(1+v_0)(1-2v_0)}\delta_{ij}\delta_{kl} + \frac{E}{2(1+v_0)}\left(\delta_{ik}\delta_{jl} + \delta_{il}\delta_{jk}\right), \tag{7}$$

where δ_{ik} is the Kronecker delta.

The $S_{ijkl}(\boldsymbol{r})$ is the Eshelby tensor outside the twin crystal. For convenience, when $S_{ijkl}(\boldsymbol{r})$ is derived, the twin crystal is set to $a_1 < a_2 = a_3$ where a_1, a_2 and a_3 are the semi-axes of the ellipsoid, and the aspect ratio $A = a_2/a_1$. The input parameters of $S_{ijkl}(\boldsymbol{r})$ are the size of the twin crystal, i.e., a_1, a_2, a_3, and v_0. The size of an isolated twin crystal should be larger than its critical size. For example, when the applied stress is 100 MPa tensile stress along [0001] of the Mg matrix, the critical size of the homogeneously formed twin crystal is $a_1 = 3.00 \times 10^{-2}$ μm, $a_2 = a_3 = 2.40$ μm. Hence, A = 80:1. The detailed calculation of the critical size is given in Appendix 1, and the completed form of $S_{ijkl}(\boldsymbol{r})$ is given in Appendix 2. Note that when $\boldsymbol{r}$ locates inside the twin crystal, $S_{ijkl}(\boldsymbol{r})$ degenerates to the classical Eshelby's tensor, S^{0}_{ijkl} [56–58], and becomes independent of $\boldsymbol{r}$. Thus, $\boldsymbol{\sigma}^{\mathbf{in}}$ also becomes independent of $\boldsymbol{r}$, and represents the back-stress inside the twin crystal. The form of S^{0}_{ijkl} is also given in Appendix 2.

4.2 Effects of stress fields of IPT/ST on the variant selection of ST/IPT

As IPT and ST form a twin pair, we consider first how the stress at the tip of one twin affects the formation of the other. From the present experimental data, it is difficult to determine whether IPT or ST forms first, and we will thus consider both cases. If IPT forms first, whether the stress field of the IPT belonging to variant V*i*, i.e., $\boldsymbol{\sigma}^{\mathbf{IPT}}(\mathrm{V}i)$, favours the formation of ST belonging to variant V*ij* can be judged by the calculation results of Eq. 5, when $\boldsymbol{\sigma}$ and $\boldsymbol{\varepsilon}^{\mathbf{p}}$ are substituted by $\boldsymbol{\sigma}^{\mathbf{IPT}}(\mathrm{V}i)$ and SFTS of V*ij*, $\boldsymbol{\varepsilon}^{\mathbf{ij}}$. Special attention is paid to the distribution of interaction energy on twin planes, as twin crystals prefer to grow along their twin planes. The detailed calculation process is provided in

Appendix 3. For type I IPT–ST pair, e.g., V2–V12, the elastic strain energy caused by $\boldsymbol{\sigma}^{\mathbf{IPT}}(\mathrm{V2})$ can be relaxed by the formation of the secondary twin variant V12, i.e., the formation of V12 is energetically favoured. This is reflected by the negative interaction energy distributed on the twin plane of V12 (the blue region in Fig. 6a). Compared with other regions, inside RPT (V1), V12 is more favoured to nucleate near the intersection line *MN* because the most negative interaction energy distributes along the intersection line, with a magnitude of around -8.0×10^7 J/m^3. This is reasonable since the stress generated by a twin crystal is concentrated at its rim.

If the ST crystal V12 forms first, to evaluate whether the stress field of V12, $\boldsymbol{\sigma}^{\mathbf{ST}}(\mathrm{V12})$, favours the formation of the IPT variant V1, the distribution of the interaction energy between $\boldsymbol{\sigma}^{\mathbf{ST}}(\mathrm{V12})$ and the SFTS of V1, $e^{\mathrm{int}}(\mathrm{V12-V1})$, on the twin plane of V1 is shown in Fig. 7. It is found that the formation of IPT V2 is also favoured by the stress field of the ST V12, as the values of $e^{\mathrm{int}}(\mathrm{V12-V1})$ are negative at the twin plane of V2. The most negative interaction energy is again approximately -8.0×10^7 J/m^3. Thus, the formation of V2–V12 pair is energetically favoured, as demonstrated by the calculation results shown in Fig. 6a and Fig. 7, i.e., the elastic strain energy caused by the stress field of V2 can be relaxed by V12, and vice versa. This can easily be understood because the interaction energy is a parameter that can be used to judge whether two twins are mutually favourable. In other words, regardless of the formation sequence of the two twins (either IPT or ST forms first), interaction energy calculation results indicate whether forming adjoining twin pairs will reduce the total energy of the system, i.e., whether the formation of the adjoining twin pairs is favoured.

If the intersection line between the twin planes of IPT and RPT is different from that between the RPT and ST, i.e., the situation that the twin planes of IPT–ST pairs only have a point contact, the influence of the stress field of IPT is tiny and only limited to the small region near the contacting point. One example is the V2–V1–V14 configuration shown in Fig. 6b. In this case, values of the interaction energy are close to 0 for the major part in the V14 twin plane. The largest absolute values of the interaction energy are concentrated in the small region near the connecting point *O* of the two intersection lines (*MN* and *PQ* in Fig. 6b), but these values decrease rapidly with increasing distance from the point *O*. Therefore, the influence of the stress field of IPT on the formation of ST is much more effective when the intersection line between the twin planes of IPT and RPT is the same as that between the RPT and ST.

Besides Type I twin-twin interactions, for each of the Type II and III interaction twin pairs, there also exists a ST variant that intersects the twin planes of IPT and RPT at a common line (see Figs. 3e and 3f). As shown in Fig. 3e, the twin plane of ST variant V13 intersects that of the IPT V3 and RPT V1 at a common line that is parallel to $[\bar{2}201]$ of the matrix, then compose a V3–V1–V13 configuration (type II). In this case, values of the interaction energy between the stress field of V3 and SFTS of V13, are positive on the twin plane of V13 (see the region in red in Fig. 6c). Thus, the stress field of V3 cannot be relaxed by V13, i.e., the V3–V13 pair (Type II) is energetically *not* favoured in terms of elastic strain energy. Similarly, if V13 forms first, the stress field of V13 does not favour the formation of V3, which will not be discussed further. For the type III IPT–ST pair given in Fig. 3f, only V14 intersects the intersecting (V4) and recipient (V1) twins at a common line. In this case, values of the interaction energy between the stress field of V4 and the SFTS of V14 on the twin plane of V14 are again positive (Fig. 6d), and thus, the Type III V4–V14 pair is not favoured either.

Among the three types of IPT–ST pairs, only the formation of the Type I IPT–ST pair is energetically favoured, i.e., the stress field of the IPT favours the formation of ST, and vice versa. This type of IPT–ST pair is exactly the one that is observed experimentally in this work (Section 3) and previous works [12, 17, 21, 22]. Thus, the calculation results well explain why only this specific type of IPT–ST pair is present. All possible IPT–RPT combinations that may result in the formation of an IPT–RPT–ST structure are investigated. In terms of crystallography, there are 30 IPT–RPT combinations in total, i.e., V*i*–V*j*, $i, j = 1 - 6$ and $i \neq j$. Among these combinations, 12 of them are crystallographically equivalent and belong to Type I, i.e., these IPT–RPT intersections may compose Type I IPT–RPT–ST configuration together with a proper ST variant according to interaction energy calculation results performed in this section. All 30 IPT–RPT combinations, and the ST variants that

can form Type I IPT–RPT–ST configuration, are listed in Table 6. In total, 12 combinations of Type I IPT-RPT-ST configuration are possible.

4.3 Effects of back-stress inside RPT on the variant selection of ST

The ST crystals are always embedded in RPT crystals. Inside a RPT crystal of variant Vi, whether the formation of a ST crystal of variant Vij is favoured by the back-stress of the RPT, $\boldsymbol{\sigma}^{\mathbf{RPT}}(\mathrm{V}i)$, i.e., the internal stress of RPT, can also be judged by Eq. 5, in which the $\boldsymbol{\sigma}$ and $\boldsymbol{\varepsilon}$ are substituted by $\boldsymbol{\sigma}^{\mathbf{RPT}}(\mathrm{V}i)$ and $\boldsymbol{\varepsilon}^{\mathbf{ij}}$, respectively. Note that $\boldsymbol{\sigma}^{\mathbf{RPT}}(Vi)$ is independent of position $\boldsymbol{r}$ and can be calculated by Eqs. 6b, A29 and A30. From Eqs. A29 and A30, it is easy to find that the absolute values of non-zero components in $\boldsymbol{\sigma}^{\mathbf{RPT}}$ increase when the aspect ratio of the RPT crystal decreases.

If a RPT crystal is variant V1, and the aspect ratio of the RPT crystal is set to 80:1, the values of interaction energies between the $\boldsymbol{\sigma}^{\mathbf{RPT}}(\mathrm{V1})$ and the SFTSs of all 5 ST variants potentially formed in RPT V1, i.e., V1j (j=2– 6), are negative (Table 7). Thus, the formation of all ST variants is favoured by the internal stress of RPT. But these values are in the order of 10^6 J/m^3, which is an order of magnitude lower than the values of interaction energy between the stress field of IPT (V2) that also has a 80:1 aspect ratio and the SFTS of V12, i.e., $e^{\mathrm{int}}(\mathrm{V2-V12})$, near the IPT–ST intersection line, which is in the order of 10^7 J/m^3, see Fig. 6a.

When the aspect ratio of RPT is reduced to 8:1, values of the interaction energy between $\boldsymbol{\sigma}^{\mathbf{RPT}}(\mathrm{V1})$ and SFTS of ST (V12), $e^{\mathrm{int}}(\mathrm{V1-V12})$, is -3.79×10^7 J/m^3, which is still less negative but at least in the same order of magnitude of the value of $e^{\mathrm{int}}(\mathrm{V2—V12})$ ($\sim -8.0\times10^7$ J/m^3). This means that only when the aspect ratio of the RPT is less than 1/10 of that of IPT, i.e., RPT is 10 times thicker than IPT if their lengths are the same, the internal stress of RPT is comparable with the stress concentrated at the rim of IPT near the IPT–ST intersection line. For the experimentally observed IPT–RPT–ST configurations, although RPT and IPT may have different aspect ratios, a difference of 10 times is rare, and thus, the influence of the internal stress of the RPT on the variant selection of the ST is less than the stress field concentrated at the tip of the IPT.

But it is worth to emphasize that the internal stress in RPT plays an important role in the growth of ST crystals as the internal stress distributes uniformly in the whole RPT, while the stress of IPT only concentrates on a local region near the IPT–ST intersection line. This is further illustrated in Fig. 8. This figure shows that the value of $e^{\mathrm{int}}(\mathrm{IPT—ST})$ increase dramatically as the distance to the intersection line increases while that of $e^{\mathrm{int}}(\mathrm{RPT—ST})$ is a constant. The critical distance is 0.23 μm, which means that, when the distance to the intersection line is larger than this critical distance, the value of $e^{\mathrm{int}}(\mathrm{IPT—ST})$ is larger than that of $e^{\mathrm{int}}(\mathrm{RPT—ST})$. Thus, influence of $\boldsymbol{\sigma}^{\mathbf{IPT}}$ on the ST becomes smaller than $\boldsymbol{\sigma}^{\mathbf{RPT}}$. The influence of $\boldsymbol{\sigma}^{\mathbf{RPT}}$ becomes larger when the aspect ratio of RPT decrease to 8:1 (see the brown line). In this case, $e^{\mathrm{int}}(\mathrm{RPT—ST})$ becomes more negative and the critical distance decreases to 6×10^{-3} μm.

4.4 Effects of the applied stress on the variant selection of IPT and ST

Effects of the applied stress on the variant selection of IPT and ST for the two cases analysed in Sections 3.2 and 3.3 are investigated. It is to be noted that, if the direction of the applied stress changes, the RPT crystals may not be favoured to form, and thus the formation of the ST crystals may also be influenced. Therefore, to consider the effect of the applied stress on the formation of ST, it is always necessary to discuss the effect of the applied stress on RPT at the same time.

In fact, when a uniaxial stress is applied on a sample, if the applied stress favours the formation of a RPT variant, then a ST is difficult to form inside the RPT. For example, the interaction energy between the applied stress and the SFTS of RPT (Variant V1) is:

$$e^{\mathrm{int}}(\boldsymbol{\sigma}^{\mathrm{app}} - \mathrm{V1}) = -\sigma_{ij}^{\mathrm{app}}\varepsilon_{ij}^{1} = 0.0649\sigma_{11}^{\mathrm{app}} - 0.0649\sigma_{33}^{\mathrm{app}} + 0.0086\sigma_{13}^{\mathrm{app}}\,, \qquad (8)$$

where $\boldsymbol{\sigma}^{\mathrm{app}}$ is the applied stress tensor and $\boldsymbol{\varepsilon}^{1}$ is the SFTS of twin variant V1. The form of $\boldsymbol{\varepsilon}^{1}$ is listed in Table 2 ($\varepsilon_{11}^{1} = -0.0649, \varepsilon_{33}^{1} = 0.0649$, $\varepsilon_{13}^{1} = \varepsilon_{31}^{1} = -0.0043$, and the other components of $\boldsymbol{\varepsilon}^{1}$ are 0). This equation reveals that, V1 is favoured to form under a compressive stress along $[10\bar{1}0]$ (negative σ_{11}) and/or a tensile stress along [0001] (positive σ_{33}). However, all 5 secondary twins that can potentially form inside the primary twin variant V1, i.e., V1*j* (*j* = 2–6), are not favoured to form when $\sigma_{11} < 0$ and/or $\sigma_{33} > 0$ because $\varepsilon_{11}^{1\mathrm{j}} > 0$ and $\varepsilon_{33}^{1\mathrm{j}} < 0$ (opposite sign to ε_{11}^{1} and ε_{33}^{1}), which result in a positive value of $e^{\mathrm{int}}(\boldsymbol{\sigma}^{\mathbf{app}}\text{—V1j})$. Therefore, the stress state that favours V1 cannot favour V1*j* simultaneously. It is the same for all the other twin variants. For the first case described in Section 3.2, a uniaxial tensile stress of approximately 100 MPa is applied along [0001] of the Mg matrix, which is similar to [21]. The interaction energies between the applied stress and the SFTS of all 30 ST variants are positive, i.e., $e^{\mathrm{int}}(\boldsymbol{\sigma}^{\mathbf{app}}\text{—V}ij) > 0$ (*i* = 1–6, *j* = 1–6, $i \neq j$). When *i* = 1, the values of $e^{\mathrm{int}}(\boldsymbol{\sigma}^{\mathbf{app}}\text{—V1}j)$ are listed in Table 7.

For the IPT in the uniaxial tensile deformed sample, the interaction energy values between the applied stress and SFTS of all 6 primary twin variants are equal to -6.486×10^{6} J/m^3, which is negative, and thus the formation of primary twins is favoured by the applied stress. But this value is around one tenth of the interaction energy between the stress field of ST and SFTS of IPT near the IPT–ST intersection line (~ -8.0×10^{7} J/m^3, see Fig. 7). Thus, in the presence of a pre-existing ST, the tip stress of ST plays a dominant role in the variant selection of the to-be-nucleated IPT.

For the plastically deformed single crystal case described in Section 3.3, RPT of variant V1 appears during the first loading step, while the IPT–ST pairs mainly appear during the second loading step when the sample is compressed along the *Y* axis (approximately parallel to the $[\bar{1}2\bar{1}0]$ direction of the matrix) with a strain of 0.035. According to the stress-strain curve, the compressive stress is approximately 100 MPa. Table 7 lists the interaction energy of the ST variants when the applied compressive stress is 100 MPa along $[\bar{1}2\bar{1}0]$. The interaction energy of V12, V13, V15 and V16 is almost the same and is negative, which means that the formation of these ST variants is almost equally favoured by the applied stress. This agrees well with the Schmid factor listed in Table 5. However, $e^{\mathrm{int}}(\boldsymbol{\sigma}^{\mathbf{app}}\text{—V}ij)$ is again in the level of 10^{6} J/m^3. So, when a pre-existing IPT is present, the tip stress of IPT plays again a dominant role in the variant selection of ST.

ST might be activated by the applied stress if the direction of the applied stress is changed, so that RPT can form during the first loading process, and that ST can form in the second loading process. The experiment on the single crystal sample given in Section 3.3 is an example, in which the compressive stress along $[10\bar{1}0]$ is applied first to activate V1, and then along $[\bar{1}2\bar{1}0]$ (of the matrix orientation) to activate V1*j*. By comparing the effects of the applied stress and twin tip stress, it is found that the twin tip stress determines which type of twin pair forms while the applied stress determines the appearance frequency of the IPT–ST pairs. For the single crystal sample after the second loading step (Section 3.3), the ST crystals belonging to variant V1*j* forms inside RPT V1. Both the Schmid factor and the interaction energy indicate that V12 and V13 are energetically most favoured to form, followed by V15 and V16. Fig. 5 shows that the most frequently observed IPT–ST pairs is V2–V12, followed by V6–V16. Both belongs to Type I, for which the stress fields of the IPT and the ST are mutually favoured. The appearance frequency of the V2–V12 pairs is higher than the V6–V16 pairs. This might be attribute to the fact that the Schmid factors of V2 and V12 are higher than those of V6 and V16, which indicates that the applied stress is more favoured to the formation of V2 and V12 than V6 and V16. The pairs V3–V13 and V5–V15, which belong to Type II, are rarely observed, although their Schmid factors are comparable with those of V2–V12 and V6–V16.

It is worth mentioning that, the applied stress field is distributed in the whole sample, rather than within a local area, thus, similar to the role of back-stress of RPT, the applied stress plays an important role on the growth of twin crystals.

4.5 Effects of dislocation slip on the variant selection of ST

The analytical solution applied in this work is purely elastic, and the stress relaxation due to dislocation slip is not considered. Among all slip systems in Mg, the basal slip ($\{0001\}\langle 11\bar{2}0\rangle$) is the easiest to be activated. The critical resolved shear stress (CRSS) of basal slip is lower than that required to activate $\{10\bar{1}2\}$ twinning. It is then questioned whether stress relaxation due to basal slip can influence the formation, especially the variant selection, of the ST. To answer this question, three-dimensional full field finite element (FE) simulations were performed based on the crystal plasticity theory, using a user-defined material law (UMAT routine) described in a previous study [47].

The model geometry consists of a RPT crystal and an IPT crystal (Fig. 9). Both twin crystals were embedded inside a cubic shaped matrix. The Euler angle of the matrix single crystal is taken as [0 0 0], and the IPT and RPT are V2 and V1, respectively, i.e., the same configuration as shown in Fig. 6a. The simulation was performed in two steps. First, the RPT domain underwent the twinning transformation on the $(10\bar{1}2)$ along the $[\bar{1}011]$ incrementally until the total shear strain reaches the twin shear strain in Mg (0.13). Second, the IPT domain underwent the twinning transformation on the $(01\bar{1}2)$ plane along the $[0\bar{1}11]$ direction until a total shear strain of 0.13 is reached. The boundaries of the matrix crystal were kept at a fixed position during the whole simulation. We preformed two simulations. In the first simulation, dislocation slip is inhibited, i.e., only considering the elastic effects. In the second one, basal slip is allowed in the matrix and the two twin crystals. The material parameters used in the simulation are listed in Table 8, and the hardening law of the basal slip systems is as follows:

$$\tau_c = \tau_{c0}\left(1 + \frac{\Gamma_{tot}}{\Gamma_0}\right)^n \quad , \tag{9}$$

$$\Gamma_{tot} = \int_0^t \Sigma_\alpha |\dot{\gamma}^\alpha| dt \quad , \tag{10}$$

Values of e^{int} between the IPT (V2) and the ST (V12) was computed and the results are shown in Fig. 9, in which the distribution of e^{int} values is shown in a cross-section parallel to the twin plane of the V12 and passing through the centre line of the intersection region between the RPT and IPT. In this computation, the interaction energy values are normalized, i.e., if only considering the elastic strain energy, the minimum e^{int} value is set to –1 (Fig. 9a). When basal slip is activated (Fig. 9b), e^{int} becomes around 60% of the inactivated case (Fig. 9a). The formation of secondary twin V12 is still favoured inside the RPT. The other two types of IPT–RPT intersections (represented by V3–V1 and V4–V1) are also verified by CP-FEM. All these simulations show that plastic relaxation due to basal slip does not affect the conclusion that only the Type I (V2–V1–V12) configuration is favourable.

5. Discussion

5.1 Why is the interaction energy between IPT and ST in Type I IPT–ST pair negative?

Interaction energy calculation results presented in Section 4.1 reveal that only in Type I IPT−ST pair, the stress fields of IPT and ST are mutually favoured, i.e., the interaction energy between IPT and ST is negative (see Fig. 6a and Fig. 7). To illustrate the origin of this negative interaction energy, interaction of elasticity fields between IPT and ST is qualitatively analysed. The stress field at the rim of a twin plane is equivalent to that of a dislocation loop enveloping the twin plane, which is

termed twinning dislocation in the followings. The Burgers vector $\boldsymbol{b}$ of the twining dislocation satisfies the relationship $\boldsymbol{b}/d = \boldsymbol{s}$ where d is the distance of the neighbouring twin plane. At the intersection line between the twin planes of IPT and ST, the two twinning dislocations that correspond to IPT and ST are superimposed and their sense vectors are set parallel to $\boldsymbol{n}^{\mathbf{IPT}} \times \boldsymbol{n}^{\mathbf{ST}}$. The Burgers vectors of these two twinning dislocations, $\boldsymbol{b}^{\mathbf{IPT}}$ and $\boldsymbol{b}^{\mathbf{ST}}$, have the same magnitude b but point at different directions. Both $\boldsymbol{b}^{\mathbf{IPT}}$ and $\boldsymbol{b}^{\mathbf{ST}}$ can be decomposed to a screw component, $\boldsymbol{b}_{\mathbf{s}}^{\mathbf{IPT}}$ and $\boldsymbol{b}_{\mathbf{s}}^{\mathbf{ST}}$, which is parallel to the intersection line, and an edge component, $\boldsymbol{b}_{\mathbf{e}}^{\mathbf{IPT}}$ and $\boldsymbol{b}_{\mathbf{e}}^{\mathbf{ST}}$, which is perpendicular to the intersection line. The $\boldsymbol{b}_{\mathbf{s}}^{\mathbf{IPT}}$, $\boldsymbol{b}_{\mathbf{e}}^{\mathbf{IPT}}$, $\boldsymbol{b}_{\mathbf{s}}^{\mathbf{ST}}$ and $\boldsymbol{b}_{\mathbf{e}}^{\mathbf{ST}}$ are schematically represented in Fig. 10a, from which it is found that $\boldsymbol{b}^{\mathbf{IPT}} = \boldsymbol{b}_{\mathbf{s}}^{\mathbf{IPT}} + \boldsymbol{b}_{\mathbf{e}}^{\mathbf{IPT}}$ and $\boldsymbol{b}^{\mathbf{ST}} = \boldsymbol{b}_{\mathbf{s}}^{\mathbf{ST}} + \boldsymbol{b}_{\mathbf{e}}^{\mathbf{ST}}$, and the magnitude of these vectors should satisfy $|\boldsymbol{b}_{\mathbf{s}}^{\mathbf{IPT}}|^2 + |\boldsymbol{b}_{\mathbf{e}}^{\mathbf{IPT}}|^2 = |\boldsymbol{b}_{\mathbf{s}}^{\mathbf{ST}}|^2 + |\boldsymbol{b}_{\mathbf{e}}^{\mathbf{ST}}|^2 = b^2$. Exploring the interaction of these two twinning dislocations at the intersection line is an effective way to analyse the elastic interaction of IPT and ST.

For Types I and II IPT−ST pairs, the condition that $\boldsymbol{b}_{\mathbf{s}}^{\mathbf{IPT}} = -\boldsymbol{b}_{\mathbf{s}}^{\mathbf{ST}}$ is satisfied. Thus, the screw component of $\boldsymbol{b}^{\mathbf{IPT}}$ can be cancelled by that of $\boldsymbol{b}^{\mathbf{ST}}$. For the Type I IPT−ST pair, this cancellation plays a dominant role in the interaction between the two twinning dislocations because $|\boldsymbol{b}_{\mathbf{s}}^{\mathbf{IPT}}| = |\boldsymbol{b}_{\mathbf{s}}^{\mathbf{ST}}| = 0.92b$, which is far larger than $|\boldsymbol{b}_{\mathbf{e}}^{\mathbf{IPT}}|$ and $|\boldsymbol{b}_{\mathbf{e}}^{\mathbf{ST}}|$ ($|\boldsymbol{b}_{\mathbf{e}}^{\mathbf{IPT}}| = |\boldsymbol{b}_{\mathbf{e}}^{\mathbf{ST}}| = 0.39b$). Only a limited part of $\boldsymbol{b}^{\mathbf{IPT}}$ can be cancelled by $\boldsymbol{b}^{\mathbf{ST}}$ in the Type II IPT−ST pair because $|\boldsymbol{b}_{\mathbf{e}}^{\mathbf{IPT}}| = 0.62b$, which is smaller than $|\boldsymbol{b}_{\mathbf{e}}^{\mathbf{IPT}}|$ ($0.78b$). There are no screw components of the two twinning dislocations in Type III IPT−ST pair, i.e., $|\boldsymbol{b}_{\mathbf{s}}^{\mathbf{IPT}}| = |\boldsymbol{b}_{\mathbf{s}}^{\mathbf{ST}}| = 0$.

Whether the edge components of these two twinning dislocations, $\boldsymbol{l}_{\mathbf{e}}^{\mathbf{IPT}}$ and $\boldsymbol{l}_{\mathbf{e}}^{\mathbf{ST}}$, is elastically favoured depends on the angle β_e between $\boldsymbol{b}_{\mathbf{e}}^{\mathbf{IPT}}$ and $\boldsymbol{b}_{\mathbf{e}}^{\mathbf{ST}}$, which is represented in plane K in Fig. 10a and 10b. This plane is perpendicular to the intersection line and both $\boldsymbol{b}_{\mathbf{e}}^{\mathbf{IPT}}$ and $\boldsymbol{b}_{\mathbf{e}}^{\mathbf{ST}}$ locate in this plane. The tension and compression strain regions around a single edge dislocation line are marked by T and C, respectively in Fig. 10b. In this figure, the variation of the interaction of $\boldsymbol{l}_{\mathbf{e}}^{\mathbf{IPT}}$ and $\boldsymbol{l}_{\mathbf{e}}^{\mathbf{ST}}$ as a function of β_e is schematically represented. When β_e= 0º, both the tension strain and compression strain regions around $\boldsymbol{l}_{\mathbf{e}}^{\mathbf{IPT}}$ and $\boldsymbol{l}_{\mathbf{e}}^{\mathbf{ST}}$ are overlapped, which results in an increase of the total elastic energy, thus, $\boldsymbol{l}_{\mathbf{e}}^{\mathbf{IPT}}$ and $\boldsymbol{l}_{\mathbf{e}}^{\mathbf{ST}}$ are elastically unfavoured. A similar situation occurs when β_e < 90º. When β_e > 90º, the $\boldsymbol{l}_{\mathbf{e}}^{\mathbf{IPT}}$ and $\boldsymbol{l}_{\mathbf{e}}^{\mathbf{ST}}$ become elastically favoured as the tension strain field around $\boldsymbol{l}_{\mathbf{e}}^{\mathbf{IPT}}$ can be compensated by the compression strain field around $\boldsymbol{l}_{\mathbf{e}}^{\mathbf{ST}}$, and vice versa. For example, when β_e = 180º, the tension and compression strain fields around $\boldsymbol{l}_{\mathbf{e}}^{\mathbf{IPT}}$ can be fully compensated by the compression and tension strain fields around $\boldsymbol{l}_{\mathbf{e}}^{\mathbf{ST}}$. The values of β_e for Types I, II and III IPT−ST pairs are 100.0º, 34.8º and 7.4º, respectively. Thus, the strain field around $\boldsymbol{l}_{\mathbf{e}}^{\mathbf{IPT}}$ and $\boldsymbol{l}_{\mathbf{e}}^{\mathbf{ST}}$ is favourable for the Type I pair, but unfavourable for both Type II and III pairs.

For each type of IPT−ST pair, whether the elastic fields of IPT and ST are mutually favoured relates to the net effects of interaction between the edge components, and between the screw components of the two twinning dislocations that envelop a twin plane of IPT and the twin plane of ST connecting the IPT twin plane. For the Type I IPT−ST pair, the cancellation of $\boldsymbol{b}_{\mathbf{s}}^{\mathbf{IPT}}$ and $\boldsymbol{b}_{\mathbf{s}}^{\mathbf{ST}}$ ($\boldsymbol{b}_{\mathbf{s}}^{\mathbf{IPT}} = -\boldsymbol{b}_{\mathbf{s}}^{\mathbf{ST}}$) plays a dominant role. Furthermore, the elastic field of $\boldsymbol{l}_{\mathbf{e}}^{\mathbf{IPT}}$ is favoured by that of $\boldsymbol{l}_{\mathbf{e}}^{\mathbf{ST}}$. Thus, the elasticity fields of IPT and ST are mutually favoured, which is consistent with interaction energy calculation results (Fig. 6a and Fig. 7). For Type II IPT−ST pair, even though $\boldsymbol{b}_{\mathbf{s}}^{\mathbf{IPT}}$ can also be cancelled by $\boldsymbol{b}_{\mathbf{s}}^{\mathbf{ST}}$, the elasticity field of $\boldsymbol{l}_{\mathbf{e}}^{\mathbf{IPT}}$ is not favoured by that of $\boldsymbol{l}_{\mathbf{e}}^{\mathbf{ST}}$. In this case, the net effect should be quantitatively examined by interaction energy calculation results, which reveals that the elasticity field of IPT is not favoured by that of ST (Fig 6c). This is reasonable as $|\boldsymbol{b}_{\mathbf{e}}^{\mathbf{IPT}}| > |\boldsymbol{b}_{\mathbf{s}}^{\mathbf{IPT}}|$ and $|\boldsymbol{b}_{\mathbf{e}}^{\mathbf{ST}}| > |\boldsymbol{b}_{\mathbf{s}}^{\mathbf{ST}}|$. For the Type III IPT−ST pair, there is no screw component of $\boldsymbol{b}^{\mathbf{IPT}}$ and $\boldsymbol{b}^{\mathbf{ST}}$, i.e., $|\boldsymbol{b}_{\mathbf{s}}^{\mathbf{IPT}}| = |\boldsymbol{b}_{\mathbf{s}}^{\mathbf{ST}}| = 0$, and the value of β_e is the smallest among the three types of IPT−ST pairs. Thus, this type is elastically most unfavoured, which is consistent with the most positive interaction energy (Fig. 6d).

5.2 Why the variant selection of IPT–ST pairs cannot be predicted by m' ?

In previous sections, we analysed the variant selection of IPT–ST pairs in deformed polycrystalline and single crystal Mg samples. The formation of the IPT–ST pair can be considered as a special type of twin transmission. But the variant selection of IPT–ST pair cannot be predicted by *m'*. To understand the reason, the physics behind *m'* and the applicable range of *m'* should be investigated.

We start from a general twin transmission case, i.e., a twin pair forming across an arbitrary grain boundary, which is schematically shown in Fig. 11a. In this case, the incoming twin with a twin shear $\boldsymbol{s}$ along an arbitrary direction is located in the grain designated *A*, which stimulates the outgoing twin with a twin shear $\boldsymbol{s'}$ in the neighbouring grain *B* and $|\boldsymbol{s}| = |\boldsymbol{s'}| = s_0$. The orientations of grain *B* and the outgoing twin can be obtained by rotating an angle θ around an arbitrary rotation axis $\boldsymbol{k}$ from the orientations of grain *A* and the incoming twin, respectively. The intersection line between the twin planes of incoming and outgoing twin crystals is set at the grain boundary between grains *A* and *B*, otherwise the influence of the incoming twin to the formation of outgoing twin is tiny, see Fig. 6b. The contribution of the stress field of the incoming twin, $\boldsymbol{\sigma}^{\mathbf{it}}$, to the resolved shear stress (RSS) of the outgoing twin, is the projection of $\boldsymbol{\sigma}^{\mathbf{it}}$ to the stress component *1'2'* expressed in the *1'2'3'* system (Fig. 11a), which is the stress component on the twin plane along the twin shear direction of the outgoing twin:

$$\sigma^{\mathrm{RSS}} = R_{1'm} R_{2'n} \sigma^{\mathrm{it}}_{mn}\,, \tag{11}$$

where σ^{RSS} is the RSS of the outgoing twin, $\boldsymbol{R}$ is the rotation matrix operating from grain *A* to grain *B*, which is a function of rotation axis $\boldsymbol{k}$ and rotation angle θ:

$$\boldsymbol{R} = \begin{bmatrix} \cos\theta + k_1^2(1-\cos\theta) & -\sin\theta\cdot k_3 + k_1k_2(1-\cos\theta) & \sin\theta\cdot k_2 + k_1k_3(1-\cos\theta) \\ \sin\theta\cdot k_3 + k_1k_2(1-\cos\theta) & \cos\theta + k_2^2(1-\cos\theta) & -\sin\theta\cdot k_1 + k_2k_3(1-\cos\theta) \\ -\sin\theta\cdot k_2 + k_1k_3(1-\cos\theta) & \sin\theta\cdot k_1 + k_2k_3(1-\cos\theta) & \cos\theta + k_3^2(1-\cos\theta) \end{bmatrix}. \tag{12}$$

where k_1, k_2, k_3 is the projection of $\boldsymbol{k}$ on *1*, *2* and *3* axes in the *123* coordinate system, and $\boldsymbol{k}$ is a unit vector. By considering the physics behind $\boldsymbol{R}$, $\boldsymbol{R}$ can also be written as:

$$\boldsymbol{R} = \begin{bmatrix} l_{1'1} & l_{1'2} & l_{1'3} \\ l_{2'1} & l_{2'2} & l_{2'3} \\ l_{3'1} & l_{3'2} & l_{3'3} \end{bmatrix}, \tag{13}$$

where $l_{p'q}$ represents the cosine of the angle between the axis *p'* (*p' = 1', 2', 3'*) and the axis *q* (*q = 1, 2, 3*). By substituting Eq. 13 to Eq. 11, then,

$$\begin{aligned} \sigma^{\mathrm{RSS}} = {} & l_{1'1}l_{2'1}\sigma^{\mathrm{it}}_{11} + l_{1'1}l_{2'2}\sigma^{\mathrm{it}}_{12} + l_{1'1}l_{2'3}\sigma^{\mathrm{it}}_{13} + l_{1'2}l_{2'1}\sigma^{\mathrm{it}}_{21} + l_{1'2}l_{2'2}\sigma^{\mathrm{it}}_{22} + l_{1'2}l_{2'3}\sigma^{\mathrm{it}}_{23} + l_{1'3}l_{2'1}\sigma^{\mathrm{it}}_{31} \\ & + l_{1'3}l_{2'2}\sigma^{\mathrm{it}}_{32} + l_{1'3}l_{2'3}\sigma^{\mathrm{it}}_{33}. \end{aligned} \tag{14}$$

Note that *1/1'* and *2/2'* represents the twin plane normal and twin shear directions of incoming / outgoing twins. The coefficient of the term $l_{1'1}l_{2'2}\sigma^{\mathrm{it}}_{12}$, i.e., $l_{1'1}l_{2'2}$, is exactly the form of *m'* because $l_{1'1}$ and $l_{2'2}$ are the cosine of the angles between the twin plane normal, and between the twin shear directions, of incoming and outgoing twins, respectively. Indeed, *m'* describes the contribution of $\sigma^{\mathrm{it}}_{12}$, the shear stress on the twin plane along the twin shear direction of the incoming twin, to the RSS of the outgoing twin. Thus, *m'* is effective only when the value of $m'\sigma^{\mathrm{it}}_{12}$ is much larger than other terms in Eq. 14, i.e., $\sigma^{\mathrm{RSS}} \approx m'\sigma^{\mathrm{it}}_{12}$.

To achieve this requirement, either the magnitude of $\sigma^{\mathrm{it}}_{12}$ is much larger than other components of $\boldsymbol{\sigma}^{\mathbf{it}}$, or *m'* is much larger than the other coefficients before $\boldsymbol{\sigma}^{\mathbf{it}}$, such as $l_{1'1}l_{2'1}$ and $l_{1'1}l_{2'3}$, or

both conditions should be satisfied. These two conditions are examined for the case of V2−V12 pair (Type I IPT−ST twin pair, as mentioned in Section 2). For the first condition, the distribution of the $\boldsymbol{\sigma}^{\mathbf{it}}$ on the twin plane of ST, is plotted in Fig. 12. The *1* and *2* axes in Fig. 12 are set parallel to the twin plane normal and twin shear direction of IPT, respectively. Fig. 12 reveals that, near the IPT−ST intersection line, the stress levels of $\sigma_{22}^{\mathrm{it}}$, $\sigma_{12}^{\mathrm{it}}$ and $\sigma_{23}^{\mathrm{it}}$ are in the same order of magnitude. When the distance to the IPT−ST intersection line is 3×10^{-2} μm, the values of $\sigma_{22}^{\mathrm{it}}$, $\sigma_{12}^{\mathrm{it}}$ and $\sigma_{23}^{\mathrm{it}}$ are ~ −485 MPa, 360 MPa and −380 MPa, respectively. Thus, besides $\sigma_{12}^{\mathrm{it}}$, other stress components including $\sigma_{22}^{\mathrm{it}}$ and $\sigma_{23}^{\mathrm{it}}$ may also make contributions to RSS, and the first condition is not satisfied. For the second condition, by substituting Eq. 12 in Eq. 11, we get:

$$\begin{aligned}\sigma^{\mathrm{RSS}} = &\left[\cos\theta + k_1^2(1-\cos\theta)\right][\sin\theta\cdot k_3 + k_1k_2(1-\cos\theta)]\sigma_{11}^{\mathrm{it}} \\ &+ \left[\cos\theta + k_1^2(1-\cos\theta)\right]\left[\cos\theta + k_2^2(1-\cos\theta)\right]\sigma_{12}^{\mathrm{it}} \\ &+ \left[\cos\theta + k_1^2(1-\cos\theta)\right][-\sin\theta\cdot k_1 + k_2k_3(1-\cos\theta)]\sigma_{13}^{\mathrm{it}} \\ &+ [-\sin\theta\cdot k_3 + k_1k_2(1-\cos\theta)][\sin\theta\cdot k_3 + k_1k_2(1-\cos\theta)]\sigma_{21}^{\mathrm{it}} \\ &+ [-\sin\theta\cdot k_3 + k_1k_2(1-\cos\theta)]\left[\cos\theta + k_2^2(1-\cos\theta)\right]\sigma_{22}^{\mathrm{it}} \\ &+ [-\sin\theta\cdot k_3 + k_1k_2(1-\cos\theta)][-\sin\theta\cdot k_1 + k_2k_3(1-\cos\theta)]\sigma_{23}^{\mathrm{it}} \\ &+ [\sin\theta\cdot k_2 + k_1k_3(1-\cos\theta)][\sin\theta\cdot k_3 + k_1k_2(1-\cos\theta)]\sigma_{31}^{\mathrm{it}} \\ &+ [\sin\theta\cdot k_2 + k_1k_3(1-\cos\theta)]\left[\cos\theta + k_2^2(1-\cos\theta)\right]\sigma_{32}^{\mathrm{it}} \\ &+ [\sin\theta\cdot k_2 + k_1k_3(1-\cos\theta)][-\sin\theta\cdot k_1 + k_2k_3(1-\cos\theta)]\sigma_{33}^{\mathrm{it}} \quad . \end{aligned} \tag{15}$$

According to Eq. 15, only when θ is close to 0°, $\sigma_{12}^{\mathrm{it}}$ makes the major contribution on RSS as all the other coefficients before $\sigma_{mn}^{\mathrm{it}}$ are close to 0 while *m′*, i.e., $\left[\cos\theta + k_1^2(1-\cos\theta)\right]\left[\cos\theta + k_2^2(1-\cos\theta)\right]$, is close to 1. The V2−V12 pair corresponds to a rotation of θ = 180° and $\boldsymbol{k}$//$[10\bar{1}2]$, and in Eq. 15, the coefficient before $\sigma_{22}^{\mathrm{it}}$ and $\sigma_{23}^{\mathrm{it}}$ is - 0.33 and - 0.68, respectively, while that before $\sigma_{12}^{\mathrm{it}}$, i.e., *m′*, is close to 0. Thus, the second condition is not satisfied, either. Actually, according to Fig. 12 and Eq, 15, $\sigma_{22}^{\mathrm{it}}$ and $\sigma_{23}^{\mathrm{it}}$, rather than $\sigma_{12}^{\mathrm{it}}$, are the major contributors to RSS of V12. This explains why *m′* cannot predict the variant selection of V2 - V12 pairs.

5.3 Normalised resolved shear stress and normalised interaction energy

To further illustrate the applicable range of *m′*, two other coefficients, the normalised resolved shear stress, $\sigma_{\mathrm{N}}^{\mathrm{RSS}}$ and the normalised interaction energy, $e_{\mathrm{N}}^{\mathrm{int}}$ are introduced. These coefficients are obtained by normalising the RSS of the outgoing twin, and the interaction energy between the stress field of incoming twin and SFTS of outgoing twin, e^{int}, against σ_0^{RSS} and e_0^{int}, respectively, i.e., $\sigma_{\mathrm{N}}^{\mathrm{RSS}} = \sigma^{\mathrm{RSS}}/\ \sigma_0^{\mathrm{RSS}}$ and $e_{\mathrm{N}}^{\mathrm{int}} = e^{\mathrm{int}}/e_0^{\mathrm{int}}$. Note that both σ^{RSS} and e^{int} are functions of the position, and thus a representative position is selected. This representative position is chosen on the outgoing twin plane, and the distance between the representative position and the intersection line between the twin planes of incoming and outgoing twins is 3×10^{-2} μm. The σ_0^{RSS} and e_0^{int} are the values of σ^{RSS} and e^{int} when there is no rotation between the incoming and outgoing twins.$\sigma_{\mathrm{N}}^{\mathrm{RSS}}$ and $e_{\mathrm{N}}^{\mathrm{int}}$ are equivalent because $e^{\mathrm{int}} = -s_0\sigma^{\mathrm{RSS}}$ [54]. Similar to *m′*, a higher value of $\sigma_{\mathrm{N}}^{\mathrm{RSS}}$ (or equivalently, $e_{\mathrm{N}}^{\mathrm{int}}$) means that the outgoing twin is energetically more favourable to form under the influence of the stress field of an incoming twin. It is noted that although the absolute values of σ^{RSS} and e^{int} depend on the selection of representative positions, when normalized, $\sigma_{\mathrm{N}}^{\mathrm{RSS}}$ and $e_{\mathrm{N}}^{\mathrm{int}}$ are almost independent of the representative positions, and thus can be treated as parameters that only depend on the rotation between the incoming and outgoing twins. The $\sigma_{\mathrm{N}}^{\mathrm{RSS}}$ and $e_{\mathrm{N}}^{\mathrm{int}}$ are more effective than *m′*, as they directly reflect the influence of the stress fields of the incoming twin to the formation of the outgoing twin, and especially, consider all stress components.

Two cases are given to compare predictions of $\sigma_{\mathrm{N}}^{\mathrm{RSS}}$, $e_{\mathrm{N}}^{\mathrm{int}}$ and *m′*. For the first case, the rotation axis $\boldsymbol{k}$ is set parallel to $[\bar{2}110]$ of grain *A*. As θ varies from 0° to 360°, the variation of *m′* for all

ranges of θ is close to that of $\sigma_{\mathrm{N}}^{\mathrm{RSS}}$ and $e_{\mathrm{N}}^{\mathrm{int}}$ (Fig. 11b), because $\sigma_{12}^{\mathrm{it}}$ makes the major contribution on σ^{RSS} while contributions of other stress components remain negligibly small (Fig. 11c), i.e., the condition that $\sigma^{\mathrm{RSS}} \approx m'\sigma_{12}^{\mathrm{it}}$ is satisfied. Therefore, m' can effectively explain the likelihood of twin transmission for this type of rotation between the incoming and outgoing twins.

For the second case, the rotation axis is set to $[10\bar{1}2]$. There is a cut-off angle for m' to be effective to predict twin transmission, either < 100° or > 250°. When θ is in the range 0–100° and 250–360°, the variation of m' still follows approximately that of $\sigma_{\mathrm{N}}^{\mathrm{RSS}}$ and $e_{\mathrm{N}}^{\mathrm{int}}$ (Fig. 11d), because within these two ranges, $\sigma_{12}^{\mathrm{it}}$ is still the major contributor to σ^{RSS} (Fig. 11e). m' becomes less effective in prediction in the range 100–250°, because the contribution of $\sigma_{12}^{\mathrm{it}}$ to σ^{RSS} is close to 0 and even negative and other stress components become the major contributor (Fig. 11e). Thus, within the θ range of 100–250°, m' is negative, but both $\sigma_{\mathrm{N}}^{\mathrm{RSS}}$ and $e_{\mathrm{N}}^{\mathrm{int}}$ are positive and reach the local maximum when θ = 180° (Fig. 11d). In other words, when θ = 180°, both $\sigma_{\mathrm{N}}^{\mathrm{RSS}}$ and $e_{\mathrm{N}}^{\mathrm{int}}$ values suggest that the stress fields of the incoming twin favour the formation of the outgoing twin, and these two twins can form a twin pair, but m' predict that this type of twin pair cannot form. Note that, at θ = 180°, grains *A* and *B* have a twinning relationship, and the rotation between the incoming and outgoing twins is the same as that between IPT and ST in the type I IPT–ST pair, e.g., V2–V12. Therefore, the experimental results described in Section 3 give a clear evidence supporting the prediction of $\sigma_{\mathrm{N}}^{\mathrm{RSS}}$ and $e_{\mathrm{N}}^{\mathrm{int}}$. For this type of rotation, m' is not a good predictor. The above two cases demonstrate that both $\sigma_{\mathrm{N}}^{\mathrm{RSS}}$ and $e_{\mathrm{N}}^{\mathrm{int}}$ are more general than m'. In contrast, m' fails to explain the likelihood of twin transmission when $\sigma_{12}^{\mathrm{it}}$ is not the major contributor to the RSS of the outgoing twin. Except for certain special rotation axes, there exists a cut-off angle for m' to be effective and this angle depends on the rotation axis.

It is worth mentioning that, all calculations made in this section assume that the intersection line between the twin plane of the incoming twin and the grain boundary plane, and that between the twin plane of outgoing twin and the grain boundary plane, are the same, i.e., there is no misalignment between the incoming and outgoing twins at the grain boundary. This geometrical requirement of having a common intersection line is also critical in the determination whether twin transmission can occur, and which twin variant can nucleate at the tip of the incoming twin. At least, the misalignment of adjoining twins at the grain boundary should be small enough (e.g., < 10º) to allow the curved twin plate to compensate [47].

5.4 Further applications of the analytical approach

The analytical approach to calculate the stress fields around a single twin crystal and the analysis of IPT−ST twin pairs can be extended to study general twin-twin interactions. In Sections 5.2 and 5.3, the analytical approach is extended to study $\{10\bar{1}2\}$ twin transmission across ordinary grain boundaries. Twin transmission was also reported in other twinning systems and materials (e.g. [76]), and it is even possible to form a twin pair consisting of different types of twin crystals (e.g. [77]). To study twin transmission in other twinning systems, it simply requires to get the stress fields of the incoming twin by replacing the twin shear and twin normal directions, and the twin shear strain, and to recalculate the corresponding SFTS of the outgoing twin. Furthermore, this analytical approach can be extended to study elasticity fields around an inclusion formed by a solid-state phase transformation, e.g., a martensite plate or a precipitate.

6. Conclusions

In this work, an analytical approach based on Eshelby's inclusion theory is developed and applied to calculate the stress fields inside and outside an isolated twin crystal and to analyse the elastic

interactions of different twin crystals. This approach is used to study variant selection of $\{10\bar{1}2\}$ primary–secondary twin pairs that form IPT–RPT–ST configurations. The following conclusions are drawn.

- In an IPT−RPT−ST configuration, only when the twin planes of IPT, RPT and ST intersect at a common line, the stress field of the IPT can effectively interact with that of the ST. There are three IPT−RPT−ST configurations satisfying this condition, and the typical examples are V2–V1−V12 (Type I), V3–V1−V13 (Type II) and V4–V1−V14 (Type III). The type I IPT−RPT−ST configuration (and the corresponding IPT−ST pair) is more frequently observed than the other two in deformed polycrystalline and single crystal Mg samples.
- Three types of stresses may influence the variant selection of IPT and ST in an IPT−ST pair: *a*. stress concentrated at the rims of the IPT and the ST, *b*. the back-stress inside the RPT and *c*. the applied stress. The first type of stress plays a dominant role on the variant selection while the latter two types of stresses may influence the growth of secondary and primary twin crystals. Among three types of IPT−ST pairs, only in Type I pair, the stresses concentrated at the rims of IPT and ST are mutually favoured. Thus, only the formation of this type of IPT−ST pair can decrease the elastic strain energy of the sample, which explains why this type of IPT–ST pair is frequently observed experimentally.
- The following two conditions need to be fulfilled to form an adjoining twin pair: *a geometrical condition* that the intersection line of the incoming twin and the outgoing twin with the grain boundary should coincide; and *an energy condition* that forming the twin pair should reduce the elastic energy.
- For the energy condition, it is suggested to use a new coefficient, i.e., normalised interaction energy, to replace the geometrical compatibility factor, m', because m' only considers the contribution of the shear stress on the twin plane along the twin shear direction of the incoming twin to the RSS of the outgoing twin. But in some other cases, other stress components induced by the incoming twin can trigger the outgoing twins, and m' is not a good predictor for these cases.

Acknowledgments

HL acknowledges the support from the FWO and European Union's Horizon 2020 research and innovation programme under the Marie Sklodowska-Curie grant agreement No. 665501. NM and HL acknowledge the funding from the European Research Council (ERC) under the European Union's Horizon 2020 research and innovation program (INTERDIFFUSION, grant agreement no. 714754). FXL acknowledges the funding from the European Research Council (ERC grant agreement No.788567 M4D). JFN is grateful to the support from the Australian Research Council. LMP acknowledges the funding from National Nature Science Foundation of China (grant No. 51771113). LD is mandated by the FSR-FNRS Belgium. Prof. Q. Liu is highly acknowledged for providing experimental samples.

Appendix 1 Critical size of an isolated twin crystal

The critical size of an isolated twin crystal when it is homogeneously formed is selected as the size of the twin crystals. According to the classical nucleation theory, there exists a critical nucleation size when a twin crystal form. This critical nucleation size corresponds to the saddle point of the free energy surface, including the contribution of elastic strain ΔG_s, and interfacial energies Γ, and the interaction energy between the applied stress $\sigma_{ij}^{\mathrm{app}}$ and SFTS of the twin crystal, ε_{ij}.The free energy surface is approximated given by [57]:

$$\Delta G = \Gamma + \Delta G_{\mathrm{s}} V - \sigma_{ij}^{app} \varepsilon_{ij} V, \qquad \text{(A1)}$$

where

$$\Delta G_{\mathrm{s}} = -\frac{1}{2} C_{ijkl}(\varepsilon_{kl}^{\mathrm{c}} - \varepsilon_{kl})\varepsilon_{ij} \ , \tag{A2}$$

$$\varepsilon_{kl}^{c} = S_{klmn}^{0}\varepsilon_{mn} \, , \tag{A3}$$

$$\Gamma = \int_0^{\frac{\pi}{2}} (4\pi)^{\frac{1}{3}} \left(\frac{3V}{A^2}\right)^{\frac{2}{3}} A\cos t \sqrt{A^2\eta_{\mathrm{T}}^2 \sin^2 t + \eta_{\mathrm{N}}^2 \cos^2 t}\, \mathrm{d}t \ . \tag{A4}$$

where V is the volume of the twin crystal, ε_{kl}^{c} is the elastic strain tensor or constrained strain tensor, and t is an integration parameter. η_{T} is the interfacial energy between the twin plane and the matrix, and $\eta_{\mathrm{T}} = 117\ \mathrm{mJ/m^2}$ according to the first principles calculation result [78]. η_{N} is the interfacial energy between the twin tip and the matrix, and it is assumed that $\eta_{\mathrm{N}} = 2\eta_{\mathrm{T}}$ [54].

The energy surface is plotted as a function of the aspect ratio (the x axis) and the volume (the y axis) of the twin crystal. The saddle point of ΔG, which corresponds to the local minimum along the x axis and the local maximum along the y axis is identified from the energy surface [79]. The twin crystal can grow freely only when the size of a twin crystal is larger than its critical nucleation size. The critical size of the twin crystal decreases as the applied stress increases. If the applied uniaxial tensile stress is 100 MPa along the [0001] of the parent crystal, then ΔG^* = 1.41 × 10^{-12} J, and the corresponding critical size of the homogeneously formed twin crystal, i.e., the twin crystal forming without any pre-existing defects for heterogeneous nucleation of the twin, is a_1 = 3.00 × 10^{-2} μm, a_2 = a_3 = 2.40 μm. Thus, the critical aspect ratio is 80:1.

Appendix 2 The form of $S_{ijkl}(\boldsymbol{r})$

Obtaining the explicit form of $S_{ijkl}(\boldsymbol{r})$ is the key step to calculate $\sigma_{ij}(\boldsymbol{r})$. Initially, we need to set the position of the twin crystal. Here, the centre of the twin crystal is set to the origin of the Cartesian coordinate system (Fig. A1). The twin plane is set perpendicular to the x axis and the twin shear direction is set along the y axis. The position $\boldsymbol{r}$ inside the twin crystal is expressed as:

$$\frac{r_i r_i}{a_I^2} \leq 1, \tag{A5}$$

where a_I (I = 1, 2, 3) is one of the three semi-axis of the oblate spheroid. In addition, the repeated lowercase indices are summed up from 1 to 3 while uppercase indices always have the same numbers as the corresponding lowercase but are not summed up, for example, $r_k a_K = r_1 a_1$ when k = 1 while $r_k a_K = r_2 a_2$ when k = 2. The calculation system is assumed as an imaginary ellipsoid that is confocal with the oblate spheroid twin crystal (Fig. A1). A point $\boldsymbol{r}$ within the matrix is given by:

$$\frac{r_i r_i}{a_I^2 + \lambda} = 1, \tag{A6}$$

and λ is given as:

$$\lambda = \frac{r_0^2 - a_1^2 - a_2^2 + \sqrt{(r_0^2 + a_1^2 - a_2^2)^2 - 4(a_1^2 - a_2^2)r_1^2}}{2} \, , \tag{A7}$$

where r_0 is the distance between the local point $\boldsymbol{r}$ in the matrix and the origin of the coordinate system. Note that, if the point $\boldsymbol{r}$ is inside the twin crystal, then λ is set to 0; otherwise $\lambda \geq 0$. In addition, an outward normal vector $\boldsymbol{e}$ is introduced (Fig. A1). At an arbitrary point $\boldsymbol{r}$ in the matrix, $\boldsymbol{e}$ is expressed as:

$$e_i = \frac{r_i}{(a_I^2 + \lambda)\sqrt{H(\lambda)}}, \tag{A8}$$

where

$$H(\lambda) = H_i(\lambda)H_i(\lambda), \;\; H_i(\lambda) = \frac{e_i}{a_I^2 + \lambda}. \tag{A9}$$

Finally, the corresponding Eshelby tensor $S_{ijkl}(\boldsymbol{r})$ for a point outside the twin crystal can be expressed as

$$\begin{aligned} S_{ijkl}(\boldsymbol{r}) = {} & P_{IK}^{(1)}(\lambda)\delta_{ij}\delta_{kl} + P_{IJ}^{(2)}(\lambda)\left(\delta_{ik}\delta_{jl} + \delta_{il}\delta_{jk}\right) + P_I^{(3)}(\lambda)\delta_{ij}e_k e_l + P_K^{(4)}(\lambda)\delta_{kl}e_i e_j \\ & + P_I^{(5)}(\lambda)\left(\delta_{ik}e_j e_l + \delta_{il}e_j e_k\right) + P_J^{(6)}(\lambda)\left(\delta_{jk}e_i e_l + \delta_{jl}e_i e_k\right) \\ & + P_{IJKL}^{(7)}(\lambda)e_i e_j e_k e_l, \end{aligned} \tag{A10}$$

By defining the aspect ratio $A = a_2/a_1$ and set $\alpha = A^{-1}$, the $\boldsymbol{P}$ components in Eq. A10 are given by:

$$P_{11}^{(1)}(\lambda) = \left[-4v_0 - \frac{2}{\alpha^2 - 1}\right] g(\lambda) - \frac{2}{3(\alpha^2 - 1)}\rho_1^3(\lambda) + \left[4v_0 + \frac{2}{\alpha^2 - 1}\right]\rho_1(\lambda)\rho_2^2(\lambda), \tag{A11}$$

$$P_{12}^{(1)}(\lambda) = P_{13}^{(1)}(\lambda) = \left[-4v_0 + \frac{2\alpha^2 + 1}{\alpha^2 - 1}\right] g(\lambda) + \left[4v_0 - \frac{2\alpha^2}{\alpha^2 - 1}\right]\rho_1(\lambda)\rho_2^2(\lambda), \tag{A12}$$

$$P_{21}^{(1)}(\lambda) = P_{31}^{(1)}(\lambda) = \left[-2v_0 - \frac{2\alpha^2 + 1}{\alpha^2 - 1}\right] g(\lambda) - \frac{2\alpha^2}{\alpha^2 - 1}\rho_1(\lambda)\rho_2^2(\lambda), \tag{A13}$$

$$\begin{aligned} P_{22}^{(1)}(\lambda) = P_{23}^{(1)}(\lambda) = P_{32}^{(1)}(\lambda) = P_{33}^{(1)}(\lambda) \\ = \left[-2v_0 + \frac{4\alpha^2 - 1}{4(\alpha^2 - 1)}\right] g(\lambda) + \frac{\alpha^2}{2(\alpha^2 - 1)}\frac{\rho_2^4(\lambda)}{\rho_1(\lambda)}, \end{aligned} \tag{A14}$$

$$P_{11}^{(2)}(\lambda) = \left[-4v_0 + \frac{4\alpha^2 - 2}{\alpha^2 - 1}\right] g(\lambda) - \frac{2}{3(\alpha^2 - 1)}\rho_1^3(\lambda) - \left[4v_0 - \frac{4\alpha^2 - 2}{\alpha^2 - 1}\right]\rho_1(\lambda)\rho_2^2(\lambda), \tag{A15}$$

$$\begin{aligned} P_{12}^{(2)}(\lambda) = P_{13}^{(2)}(\lambda) = P_{21}^{(2)}(\lambda) = P_{31}^{(2)}(\lambda) \\ = \left[-v_0 - \frac{\alpha^2 + 2}{\alpha^2 - 1}\right] g(\lambda) - \left[2v_0 + \frac{2}{\alpha^2 - 1}\right]\rho_1(\lambda)\rho_2^2(\lambda), \end{aligned} \tag{A16}$$

$$\begin{aligned} P_{22}^{(2)}(\lambda) = P_{23}^{(2)}(\lambda) = P_{32}^{(2)}(\lambda) = P_{33}^{(2)}(\lambda) \\ = \left[2v_0 - \frac{4\alpha^2 - 7}{4(\alpha^2 - 1)}\right] g(\lambda) + \frac{\alpha^2}{2(\alpha^2 - 1)}\frac{\rho_2^4(\lambda)}{\rho_1(\lambda)}, \end{aligned} \tag{A17}$$

$$P_I^{(3)}(\lambda) = \frac{\rho^3(\lambda)}{2(1-v_0)}[1-\rho_I^2(\lambda)], \tag{A18}$$

$$P_K^{(4)}(\lambda) = \frac{\rho^3(\lambda)}{2(1-v_0)}[1-2v_0-\rho_K^2(\lambda)], \tag{A19}$$

$$P_I^{(5)}(\lambda) = \frac{\rho^3(\lambda)}{2(1-v_0)}[v_0-\rho_I^2(\lambda)], \tag{A20}$$

$$P_J^{(6)}(\lambda) = \frac{\rho^3(\lambda)}{2(1-v_0)}\left[v_0-\rho_J^2(\lambda)\right], \tag{A21}$$

$$P_{IJKL}^{(7)}(\lambda) = \frac{\rho^3(\lambda)}{2(1-v_0)}\Big\{2\left[\rho_I^2(\lambda)+\rho_J^2(\lambda)+\rho_K^2(\lambda)+\rho_L^2(\lambda)\right]+\rho_m(\lambda)\rho_m(\lambda) - \frac{4\rho_M^2(\lambda)H_m(\lambda)H_m(\lambda)}{H(\lambda)}-5\Big\}, \tag{A22}$$

where

$$g(\lambda) = \begin{cases} -\dfrac{\alpha^2}{\alpha^2-1}\dfrac{\rho_2^2(\lambda)}{\rho_1(\lambda)} + \dfrac{\alpha}{(\alpha^2-1)^{\frac{3}{2}}}\ln\left[(\alpha^2-1)^{\frac{1}{2}}\rho_2(\lambda)+\dfrac{\alpha\rho_2(\lambda)}{\rho_1(\lambda)}\right] & \alpha>1 \\ -\dfrac{\alpha^2}{\alpha^2-1}\dfrac{\rho_2^2(\lambda)}{\rho_1(\lambda)} + \dfrac{\alpha}{(\alpha^2-1)^{\frac{3}{2}}}\tan^{-1}\dfrac{\alpha}{(1-\alpha^2)^{\frac{1}{2}}\rho_1(\lambda)} & \alpha<1 \end{cases} \tag{A23}$$

and

$$\rho_I^2(\lambda) = \frac{a_I^2}{a_I^2+\lambda}\,. \tag{A24}$$

By choosing $\lambda = 0$, the Eshelby tensor for a point inside the twin crystal is independent of $\boldsymbol{r}$:

$$\mathrm{S}_{ijkl}^0 = P_{IK}^{(1)}(0)\delta_{ij}\delta_{kl} + P_{IJ}^{(2)}(0)\left(\delta_{ik}\delta_{jl}+\delta_{il}\delta_{jk}\right), \tag{A25}$$

where

$$P_{IK}^{(1)}(0) = -\frac{v_0}{2(1-v_0)}J_I(0) + \frac{1}{4(1-v_0)}\left[\frac{a_I^2}{a_I^2-a_K^2}J_I(0)+\frac{a_K^2}{a_K^2-a_I^2}J_K(0)\right], \tag{A26}$$

$$P_{IJ}^{(2)}(0) = -\frac{1}{4}\left[J_I(0)+J_J(0)\right] + \frac{1}{4(1-v_0)}\left[\frac{a_I^2}{a_I^2-a_K^2}J_I(0)+\frac{a_J^2}{a_J^2-a_I^2}J_J(0)\right], \tag{A27}$$

with

$$J_I(0) = J_I(\lambda)|_{\lambda=0},\ J_I(\lambda) = \int\frac{\rho^3(\lambda)}{a_I^2+\lambda}d\lambda. \tag{A28}$$

The calculation of $S_{klmn}(\boldsymbol{r})$ and S^0_{klmn} in Eq. A10 and Eq. A25 are coded by MATLAB based on [74]. An alternative way to express S^0_{ijkl} is given by [57–59, 61]:

$$S^0_{ijkl} = S^{00}_{ijmn} C_{mnkl} \ , \tag{A29}$$

where

$$S^{00}_{ijmn} = \frac{A^2}{8\pi} \int_0^{2\pi} d\omega \int_0^{\pi} \sin\varphi \, d\varphi \, \frac{z_i z_n M^{-1}_{jm} + z_j z_n M^{-1}_{im}}{(z_1^2 + A^2 z_2^2 + A^2 z_3^2)^{\frac{3}{2}}} \quad . \tag{A30}$$

In Eq. A30, $M_{jm} = C_{ijml} z_i z_l$, which is related to the Green function in the Fourier space. Both ω and φ are integration parameters, and $\boldsymbol{z} = (\sin\varphi\cos\omega, \sin\varphi\sin\omega, \cos\varphi)$.

Appendix 3 Calculation of interaction energy at a local twin junction region

To determine the distribution of interaction energy between the stress induced by IPT and the SFTS of ST, the calculation is performed in a coordinate system defined as $x//\boldsymbol{n}^{\mathbf{IPT}}$, $y//\boldsymbol{s}^{\mathbf{IPT}}$ and $z//(\boldsymbol{n}^{\mathbf{IPT}} \times \boldsymbol{s}^{\mathbf{IPT}})$ (Fig. A2). All the twin plane normal directions, twin shear directions and SFTS of the STs listed in Table 2 are transformed to the *xyz* coordinate system. Both IPT and ST are assumed to be oblate ellipsoids, and the center of the IPT crystal is placed at the origin of the coordinate system. The coordinate of the contact point *P* (Fig. A2) between IPT and ST is determined as follows: First, the vector parallel to the intersection line between the twin planes of IPT and ST, $\boldsymbol{L1}$, is defined as $\boldsymbol{n}^{\mathbf{IPT}} \times \boldsymbol{n}^{\mathbf{ST}}$. Then, the vector that points from the center of the IPT to *P*, $\boldsymbol{L2}$, is $\boldsymbol{L2} = \boldsymbol{L1} \times \boldsymbol{n}^{\mathbf{ST}}$. Lastly, the coordinate of point *P* is given by $r \cdot \boldsymbol{L2}$, where *r* is the half length of the major axes of the IPT ellipsoid. The twin edge where IPT triggers ST is defined as the region around the contact point, (i.e., point *P* in Fig. A2). The interaction energy is calculated in a small cubic region ($0.12\times 0.12\times 0.12$ μm^3) around the point *P* and the grid size is $160\times160\times160$. Similar method can be used for the situation that ST triggers IPT by setting the center of the ST at the origin of the coordinate system, and performing the calculation in the coordinate system $x//\boldsymbol{n}^{\mathbf{ST}}$, $y//\boldsymbol{s}^{\mathbf{ST}}$, and $z//(\boldsymbol{n}^{\mathbf{ST}} \times \boldsymbol{s}^{\mathbf{ST}})$.

References

[1] J. F. Nie, K. S. Shin, Z. R. Zeng, Microstructure, deformation, and property of wrought magnesium alloys, Metall. Mater. Trans. A 51 (2020) 6045−6109.

[2] J. F. Nie, Y. M. Zhu, J. Z. Liu, X. Y. Fang, Periodic segregation of solute atoms in fully coherent twin boundaries. Science 340 (2013) 957−960.

[3] C. Roberts, Magnesium and its alloys, John Wiley & Sons, 1st Ed., New York, 1960.

[4] J. Zhang, S. P. Joshi, Phenomenological crystal plasticity modelling and detailed micromechanical investigations of pure magnesium. J. Mech. Phys. Solid. 60 (2012) 945−973.

[5] X. Liao, J. Wang, J. F. Nie, Y. Jiang, P. Wu, Deformation twinning in hexagonal materials. MRS Bulletin, 41 (2016) 314–319.

[6] P. G. Partridge, The crystallography and deformation modes of hexagonal close-packed metals, Metal. Rev. 12 (1967) 169–194.

[7] J. W. Christian, S. Mahajan, Deformation twinning, Prog. Mater. Sci. 39 (1995) 1–157.

[8] M. R. Barnett, Twinning and the ductility of magnesium alloys Part I: "Tension" twins, Mater. Sci. Eng. A, 464 (2007) 1−7.

[9] H. El Kadiri, C. D. Barrett, J. Wang, C. N. Tomé, Why are $\{10\bar{1}2\}$ twins profuse in magnesium? Acta Mater. 85 (2015) 354–361.

[10] K. D. Molodov, T. Al-Samman, D. A. Molodov, S. Korte-Kerzel, On the twinning shear of $\{10\bar{1}2\}$ twins in magnesium – Experimental determination and formal description, Acta Mater. 134 (2017) 267–273.
[11] Y. R. Paudel, J. Indeck, K. Hazeli, M. W. Priddy, J. Inal, H. Rhee, C. D. Barrett, W. R. Whittington, K. R. Limmer, H. El Kadiri, Characterization and modeling of $\{10\bar{1}2\}$ twin banding in magnesium. Acta Mater. 183 (2020) 438–451.
[12] E. Roberts, P. G. Partridge, The accommodation around $\{10\bar{1}2\}\langle10\bar{1}1\rangle$ twins in magnesium, Acta Metall. 14 (1966) 513−527.
[13] M. Z. Bian, K. S. Shin, $\{10\bar{1}2\}$ twinning behaviour in magnesium single crystals, Met. Mater. Int. 19 (2013) 999−1004.
[14] Q. Yu, J. Wang, Y. Jiang, R. J. McCabe, N. Li, C. N. Tome, Twin–twin interactions in magnesium. Acta Mater. 77 (2014) 28−42.
[15] A. Jager, A. Ostapovets, P. Molnar, P. Lejcek, $\{10\bar{1}2\}$ – $\{10\bar{1}2\}$ double twinning in magnesium, Philos. Mag. Lett. 91 (2011) 537−544.
[16] J. Jain, J. Zou, C.W. Sinclair, W.J. Poole, Double tensile twinning in a Mg–8Al–0.5Zn alloy, J. Microsc. 242 (2011) 26−36.
[17] Z. Z. Shi, Secondary twin variant selection in Mg alloy after a strain-path change. J. Alloys Compd. 696 (2017) 510−515.
[18] S. H. Park, S. G. Hong, J. H. Lee, C. S. Lee, Multiple twinning modes in rolled Mg–3Al–1Zn alloy and their selection mechanism Mater. Sci. Eng. A 532 (2012) 401−406.
[19] S. H. Park, S. G. Hong, C. S. Lee, In-plane anisotropic deformation behavior of rolled Mg–3Al–1Zn alloy by initial $\{10\bar{1}2\}$ twins Mater. Sci. Eng. A 570 (2013) 149−163.
[20] Z. X. Long, T. M. Liu, Y. G. Wu, Y. Zhang, Improving the anisotropy of rolled Mg–3Al–1Zn alloy by pre-strain and annealing Mater. Sci. Eng. A 616 (2014) 240 −245.
[21] R. Xin, C. Guo, J. J. Jonas, G. Chen, Q. Liu, Variant selection of $\{10\bar{1}2\}-\{10\bar{1}2\}$ double twins during the tensile deformation of an AZ31 Mg alloy. Mater. Sci. Eng. A 700 (2017) 226−233.
[22] Z. Z. Shi, J. Y. Xu, J. Yu, X. F. Liu, Intragranular cross-level twin pairs in AZ31 Mg alloy after sequential biaxial compressions, J. Alloys Compd. 749 (2018) 52−59.
[23] B. C. Suh, M. S. Shim, D. W. Kim, N. J. Kim, Twinning behavior of Mg−4Zn−1Gd alloy sheet during longitudinal tensile deformation, Scripta Mater. 69 (2013) 465−468.
[24] Z. Z. Shi, Y. Zhang, F. Wagner, T. Richeton, P. A. Juan, J. S. Lecomte, L. Capolungo, S. Berbenni, Sequential double extension twinning in a magnesium alloy: Combined statistical and micromechanical analyses, Acta Mater. 96 (2015) 333−343.
[25] L. Tan, X. Zhang, T. Xia, Q. Sun, G. Huang, R. Xin, Q. Liu, $\{10\bar{1}2\}-\{10\bar{1}2\}$ double tensile twinning in a Mg-3Al-1Zn alloy sheet during cyclic deformation. Mater. Sci. Eng. A 711 (2018), 205–211.
[26] Y. Xin, X. Zhou, L. Lv, Q. Liu, The influence of a secondary twin on the detwinning deformation of a primary twin in Mg-3Al-1Zn alloy. Mater. Sci. Eng. A 606 (2014) 81–91.
[27] J. Kacher, A. M. Minor, Twin boundary interactions with grain boundaries investigated in pure rhenium, Acta Mater. 81 (2014) 1−8.
[28] I. Chelladurai, D. Adams, D. T. Fullwood, M. P. Miles, S. Niezgoda, I. J. Beyerlein, M. Knezevic, Modeling of trans-grain twin transmission in AZ31 via a neighborhood-based viscoplastic self-consistent model, Inter. J. Plast. 117 (2017) 21−32.
[29] M. A. Kumar, I. J. Beyerlein, R. J. McCabe, C. N. Tome, Grain neighbour effects on twin transmission in hexagonal close-packed materials, Nature Comm. 7 (2016) 13826.
[30] X. Hong, A. Godfrey, W. Liu, Challenges in the prediction of twin transmission at grain boundaries in a magnesium alloy, Scripta Mater. 123 (2016) 77−80.

[31] I. J. Beyerlein, L. Capolungo, P. E. Marshall, R. J. McCabe, C. N. Tome, Statistical analyses of deformation twinning in magnesium, Philos. Mag. 90 (2010) 2161−2190.
[32] A. Khosravani, D. T. Fullwood, B. L. Adams, T. M. Rampton, M. P. Miles, R. K. Mishra, Nucleation and propagation of $\{10\bar{1}2\}$ twins in AZ31 magnesium alloy, Acta Mater. 100 (2015) 202–214.
[33] H. El Kadiri, J. Kapil, A. L. Oppedal, H. G. Hector, S. R. Agnew, M. Cherkaoui, S. C. Vogel, The effect of twin-twin interactions on the nucleation and propagation of $\{10\bar{1}2\}$ twinning in magnesium, Acta Mater. 61 (2013) 3459−3563.
[34] M. Gong, S. Xu, Y. Jiang, Y. Liu, J. Wang, Structural characteristics of $\{10\bar{1}2\}$ non-cozone twin-twin interactions in magnesium, Acta Mater. 159 (2018) 65−76.
[35] M. A. Kumar, M. Gong, I. J. Beyerlein, J. Wang, C. N. Tome, Role of local stresses on co-zone twin-twin junction formation in HCP magnesium. 168 (2019) Acta Mater. 353−361.
[36] C. F. Guo, R. L. Xin, C. Ding, B. Song, Q. Liu, Understanding of variant selection and twin patterns in compressed Mg alloys sheets via combined analysis of Schmid factor and strain compatibility factor, Mater. Sci. Eng. A 700 (2017) 226−233.
[37] R. L. Xin, Y. C. Liang, C. H. Ding, C. F. Guo, B. S. Wang, Q. Liu, Geometrical compatibility factor analysis of paired extension twins in extruded Mg−3Al−1Zn alloys, Mater. Des. 86 (2015) 656−663.
[38] H. Kwon, H. Nakano, M. Mabuchi, Y. Chino, Twining behaviour of AZ31 Mg alloy after alternatively compressed in two orthogonal directions, Phil. Mag. 94 (2014) 3960 –3977.
[39] Z. Z. Shi, Y. D. Zhang, F. Wagner, P. A. Juan, S. Berbenni, L. Capolungo, J. S. Lecomte, T. Richeton, On the selection of extension twin variants with low Schmid factors in a deformation Mg alloy, Acta Mater. 83 (2015) 17−28.
[40] D. Guan, B. Wynne, J. Gao, Y. Huang, W. M. Rainforth, Basal slip mediated tension twin variant selection in magnesium WE43 alloy, Acta Mater. 170 (2019) 1–14.
[41] J. Čapek, K. Máthis, B. Clausen, M. Barnett, Dependence of twinned volume fraction on loading mode and Schmid factor in randomly textured magnesium, Acta Mater. 130 (2017) 319–328.
[42] J. J. Jonas, S. Mu, T. Al-Samman, G. Gottstein, L. Jiang, E. Martin, The role of strain accommodation during the variant selection of primary twins in magnesium, Acta Mater. 59 (2011) 2046–2056.
[43] S. G. Hong, S. H. Park, C. S. Lee, Role of $\{10\bar{1}2\}$ twinning characteristics in the deformation behaviour of a polycrystalline magnesium alloy, Acta. Mater. 58 (2010) 5873−5885.
[44] M. A. Kumar, L. Capolungo, R. J. McCabe, C. N. Tome, Characterizing the role of adjoining twins at grain boundaries in hexagonal close packed materials, Sci. Rep. 9 (2019) 3846.
[45] M. A. Kumar, A. K. Kanjarla, S. R. Niezgoda, R. A. Lebensohn, C. N. Tome, Numerical study of the stress state of a eformation twin in magnesium, Acta Mater. 84 (2015) 349 −358.
[46] M. A. Kumar, I. J. Beyerlein, C. N. Tome, Effect of local stress fields on twin characteristics in HCP metals, Acta Mater. 116 (2016) 143−154.
[47] F. Lin, M. Mateleur, P. J. Jacques, L. Delannay, Transmission of {332}⟨113⟩ twins across grain boundaries in a metastable β-titanium alloy, Inter. J. Plast. 105 (2018) 195–210.
[48] C. Liu, P. Shanthraj, M. Diehl, F. Roters, S. Dong, J. Dong, W. Ding, D. Raabe, An integrated crystal plasticity–phase field model for spatially resolved twin nucleation, propagation, and growth in hexagonal materials, Inter. J. Plast. 106 (2018) 203−227.
[49] C. Liu, P. Shanthraj, J. D. Robson, M. Diehl, S. Dong, J. Dong, W. Ding, D. Raabe, On the interaction of precipitates and tensile twins in magnesium alloys, Acta Mater. 178 (2019) 146−162.

[50] H. Qiao, M. R. Barnett, P. D. Wu, Modelling of twin formation, propagation and growth in a Mg single crystal based on crystal plasticity finite element method, Int. J. Plast. 86 (2016) 70 – 92.
[51] M. R. Barnett, N. Stanford, A. Ghaderi, F. Siska, Plastic relaxation of internal stress induced twinning, Acta Mater. 61 (2013) 7859−7867.
[52] R. Y. Zhang, M. R. Daymond, R. A. Holt, Parametric study of stress state development during twinning using 3D finite modelling, Mater. Sci. Eng. A 528 (2011) 2725−2735.
[53] X. Hu, Y. Z. Ji, T. W. Heo, L. Q. Chen, X. Y. Cui, Phase field model of deformation twin-grain boundary interactions in hexagonal systems, Acta Mater. 200 (2020) 821–834.
[54] H. Liu, F. X. Lin, P. Zhao, N. Moelans, Y. Wang, J. F. Nie, Formation and autocatalytic nucleation of co-zone $\{10\bar{1}2\}$ deformation twins in polystalline Mg: a phase field simulation study. Acta Mater. 153 (2018) 86−107.
[55] F. Siska, L. Stratil, J. Cizek, A. Ghaderi, M. Barnett, Numerical analysis of twin thickening process in magnesium alloys, Acta Mater. 124 (2017) 9–16.
[56] J. D. Eshelby, The determination of the elastic field of an ellipsoidal inclusion, and related problems, Proc. R. Soc. Lond. A 241 (1957) 376−396.
[57] J. K. Lee, M. H. Yoo, Elastic strain energy of deformation twinning in tetragonal crystals, Mater. Trans. A 21 (1990) 2521−2530.
[58] M. H. Yoo, J. K. Lee, Deformation twinning in h.c.p. metals and alloys, Philos. Mag. A 63 (1991) 981−1000.
[59] R. A. Lebensohn, C. N. Tome, A study of stress state associated with twin nucleation and propagation in anisotropic materials, Philos. Mag. A 67 (1993) 187−206.
[60] J. D. Eshelby, The elastic field outside an ellipsoidal inclusion, Proc. R. Soc. Lond. A 252 (1959) 561−569.
[61] T. Mura, Micromechanics of Defects in Solids, 2nd Ed. Martinus Nijhoff, Dordrecht, The Netherlands, 1987.
[62] T. Mura, P. C. Cheng, The Elastic Field Outside an Ellipsoidal Inclusion, J. Appl. Mech. ASME 44 (1977) 591−594.
[63] J. W. Ju, L. Z. Sun, A novel formulation of the exterior-point Eshelby's tensor of an ellipsoidal inclusion, J. Appl. Mech. ASME (1999) 570–574.
[64] B. R. Kim, H. K. Lee, Closed form solution of the exterior-point Eshelby tensor for an elliptic cylindrical inclusion, J. Appl. Mech. ASME 77 (2010) 1–5.
[65] X. Jin, L. M. Keer, Q. J. Wang, A closed-form solution for the Eshelby tensor and the elastic field outside an elliptic cylindrical Inclusion, J. Appl. Mech. ASME 78 (2011) 031009.
[66] T. Joffre, A. Miettien, E. L. G. Wernersson, P. Lsaksson, E. K. Gamstedt, Effects of defects on the tensile strength of short-fibre composite materials, Mech. Mater. 75 (2014) 125−134.
[67] Q. Chen, H. Zhu, J. W. Ju, Z. W. Jiang, Z. Yan, H. X. Li, Stochastic micromechanical predictions for the effective properties of concrete considering the interfacial transition zone effects, Inter. J. Damage Mech. 27 (2018) 1252−1271.
[68] J. W. Rudnicki, Models for compaction band propagation, in Rock physics and geomechanics in the study of reservoirs and repositories, vol. 284, Geological Society, Special Publications, 2007, 107 −125.
[69] F. Bachmann, R. Hielscher, H. Schaeben, Texture Analysis with MTEX – Free and Open-Source Software Toolbox, Solid State Phenomena. 160 (2010) 63–68.
[70] C. Shen, J. P. Simmons, Y. Wang, Effect of elastic interaction on nucleation I: calculation of the strain energy nucleus formation in an elastic anisotropic crystal of arbitrary microstructure, Acta Mater. 54 (2006) 5617–5630.

[71] D. Qiu, R. Shi, D. Zhang, W. Lu, Y. Wang, Variant selections by dislocations during a precipitation in α/β titanium alloys, Acta Mater. 88 (2015) 218–231.
[72] D. Healy, Elastic field in 3D due to a spheroidal inclusion–MATLAB code for Eshelby's solution, Comput. Geosciences 2170 – 2173 (2009).
[73] U. F. Kocks, C. N. Tomé, H. R. Wenk, Texture and Anisotropy, Cambridge University Press, Cambridge 1998.
[74] Y. Liu, N. Li, S. Shao, M. Gong, J. Wang, R. J. McCabe, Y. Jiang, C. N. Tomé, Characterizing the boundary lateral to the shear direction of deformation twins in magnesium, Nature Comm. 7 (2015) 11577.
[75] Y. Liu, P. Z. Tang, M. Y. Gong, R. J. McCabe, J. Wang, C. N. Tomé, C. N. Three-dimensional character of the deformation twin in magnesium, Nature Comm. 10 (2019) 3308.
[76] J. Kacher, J. E. Sabisch, A. M. Minor, Statistical analysis of twin/grain boundary interactions in pure rhenium. Acta Mater. 173 (2019) 44–51.
[77] X. Song, J. R. Luo, Z. Z. Shi, L. Z. Zhuang, Y. Qiao, J. S. Zhang, Quantitative prediction of grain boundary misorientation effect on twin transmission in hexagonal metals. Mater. Des. 192 (2020) 108745.
[78] J. Wang, I. J. Beyerlein, Atomic structures of symmetric tilt grain boundaries in hexagonal close packed (hcp) crystlas, Model. Simulat. Mater. Sci. Eng. A 20 (2012) 024002.
[79] H. Liu, I. Papadimitriou, F. X. Lin, J. LLorca, Precipitation during high temperature ageing of Al-Cu alloys, A multiscale analysis based on first principles calculations, Acta Mater. 167 (2019) 121–135.

Figures and Tables

Figures

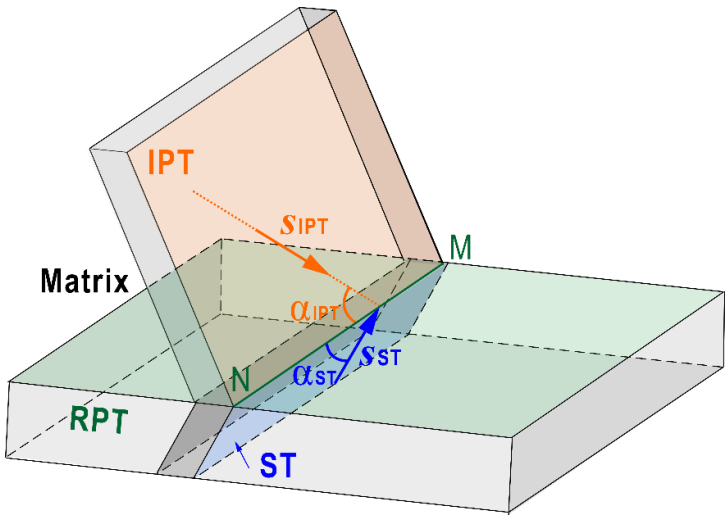

Fig. 1 Schematic diagram showing the IPT–RPT–ST configuration reported in Ref. [9]. The twin planes of the intersecting primary twin (IPT), recipient primary twin (RPT) and secondary twin (ST) are coloured orange, green and blue, respectively, and these three twin planes share a common intersection line *MN*, which is parallel to $[\bar{2}\bar{2}43]$ of the matrix. The angle between the intersection line and the twin shear direction of IPT ($\boldsymbol{s}_{IPT}$) / ST($\boldsymbol{s}_{ST}$) are marked by α_{IPT}/α_{ST}. Both α_{IPT} and α_{ST} are approximately equal to 22.83º.

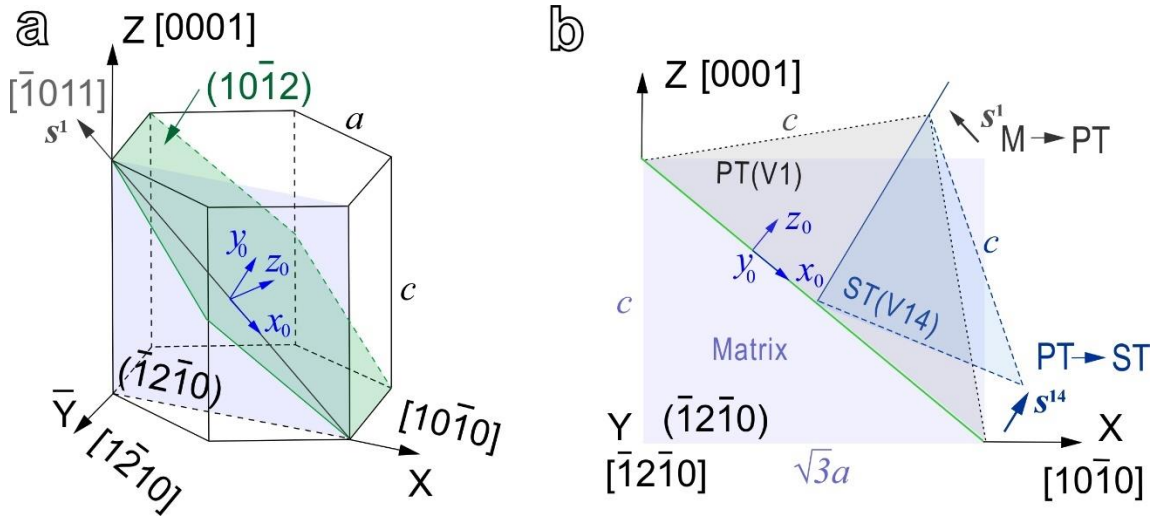

Fig. 2 (a) Schematic diagram showing the twin plane ($(10\bar{1}2)$, coloured in green) and the twin shear direction ($[\bar{1}011]$, marked by $\boldsymbol{s}^1$) of a $\{10\bar{1}2\}$ twin variant. In the $x_0y_0z_0$ coordinate system, x_0 is anti-parallel to the twin shear direction and z_0 is parallel to the normal direction of the twin plane, while in the *XYZ* coordinate system, *X*, *Y* and *Z* are parallel to $[10\bar{1}0]$, $[\bar{1}2\bar{1}0]$, and [0001] of the Mg matrix, respectively. The lattice parameters of the Mg matrix are marked by *a* and *c*. (b) Schematic diagram showing the transformation from the matrix (M) to the primary twin (PT) variant V1 (marked by M → PT) via a simple shear $\boldsymbol{s}_1$, and then to the secondary twin (ST) variant V14 (marked by PT → ST) via another simple shear $\boldsymbol{s}_{14}$. The viewing direction is perpendicular to $(\bar{1}2\bar{1}0)$. For simplicity, only the $(\bar{1}2\bar{1}0)$ plane is shown.

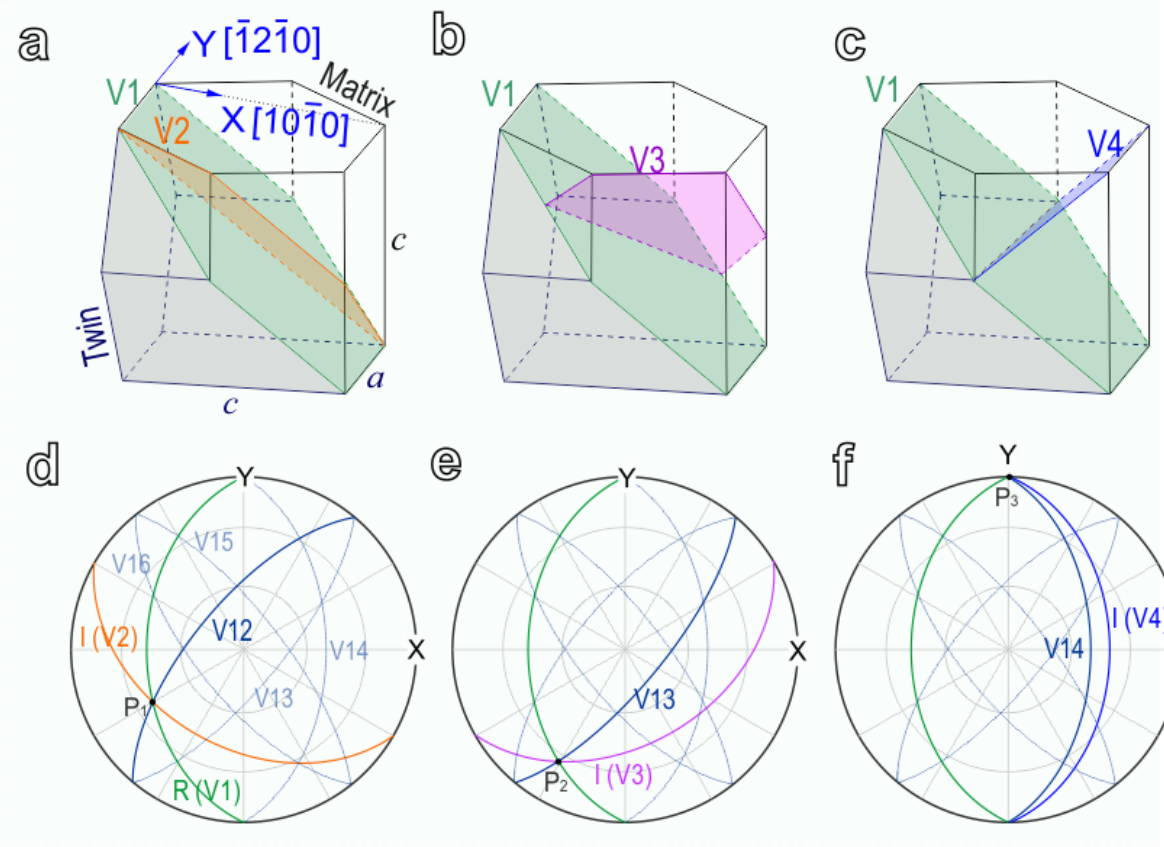

Fig. 3 (a – c) Examples of three crystallographically different types of IPT–RPT intersections: (a) Type I (V2–V1), (b) Type II (V3–V1) and (c) Type III (V4–V1). The twin plane of the RPT is coloured in green, and that of the IPT is coloured in orange in (a), purple in (b) and blue in (c). (d – f) Stereographic projections of the twin planes of IPT, RPT and ST variants. The IPT–RPT pairs in (d), (e) and (f) are V2–V1, V3–V1 and V4–V1, respectively, and the ST variants in (d – f) are V1*j* (*j* = 2–6). Note that for each IPT–RPT pair, the twin plane of only one ST variant intersects the IPT and RPT at the same line. This common intersection line is represented by P_1, P_2 and P_3 in (d), (e) and (f), respectively.

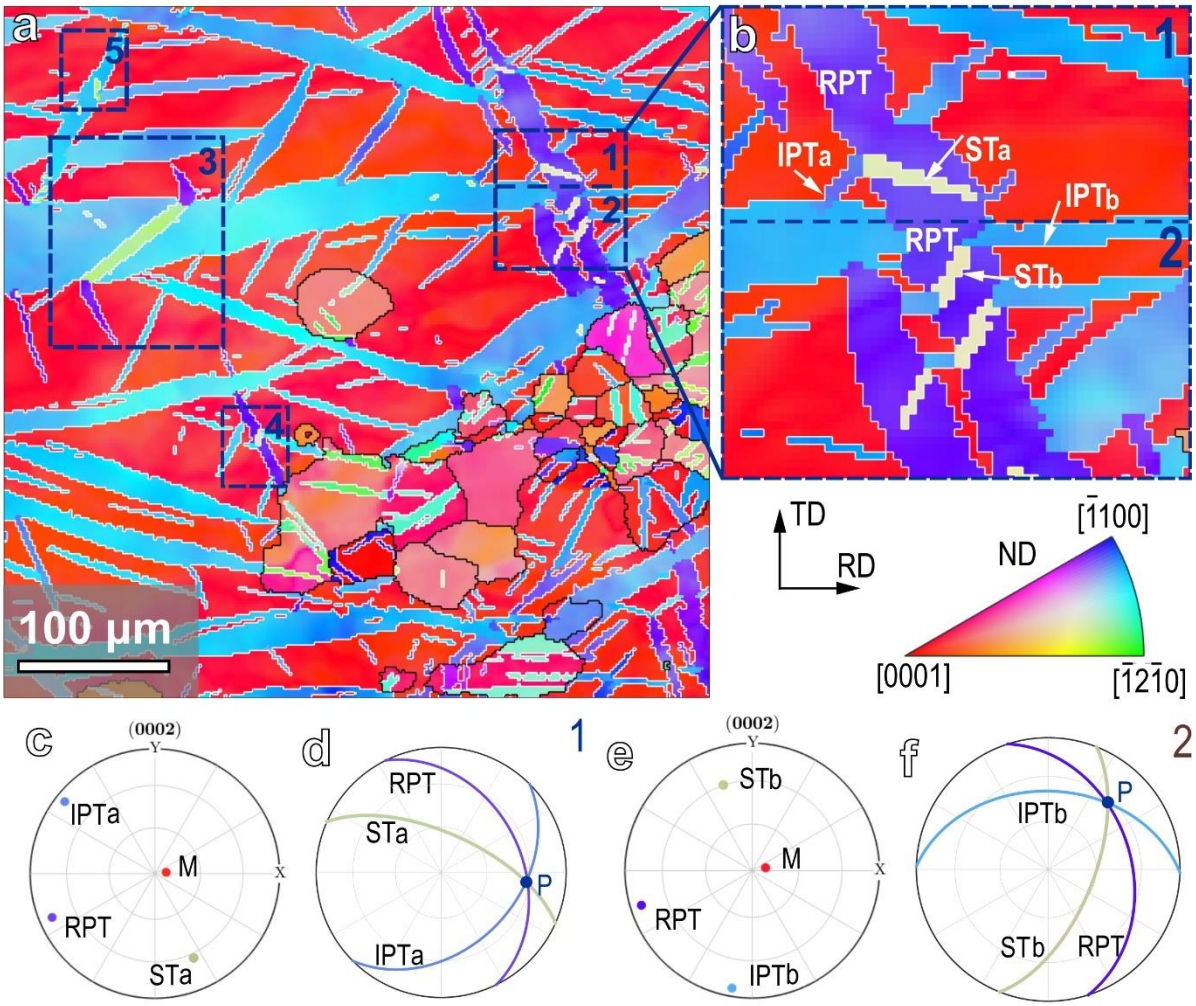

Fig. 4 Microstructure of an AZ31 sample after a tensile strain of 0.04 along ND. (a) Orientation map coloured according to the direction of the tensile loading direction. The matrix is in red, and other lamellar or lenticular shaped grains in blue or green are $\{10\bar{1}2\}$ twins. The white lines represent twin boundaries, whereas the black lines represent other types of grain boundaries. Five regions with secondary twins (ST) are marked by squares, and numbered as 1–5. (b) Enlarged view of regions 1 and 2. (c) and (e) {0002} pole figures showing orientations of the matrix (M), recipient primary twin (RPT), two intersecting primary twins (IPTa and IPTb), and the corresponding two secondary twins (STa and STb) in regions 1 and 2, respectively. The corresponding twin planes of the RPT, IPT and ST are shown in the stereographic projections (d) and (f) for regions 1 and 2, respectively. The colours representing twins and matrix in (c)–(f) are the same as those in (b).

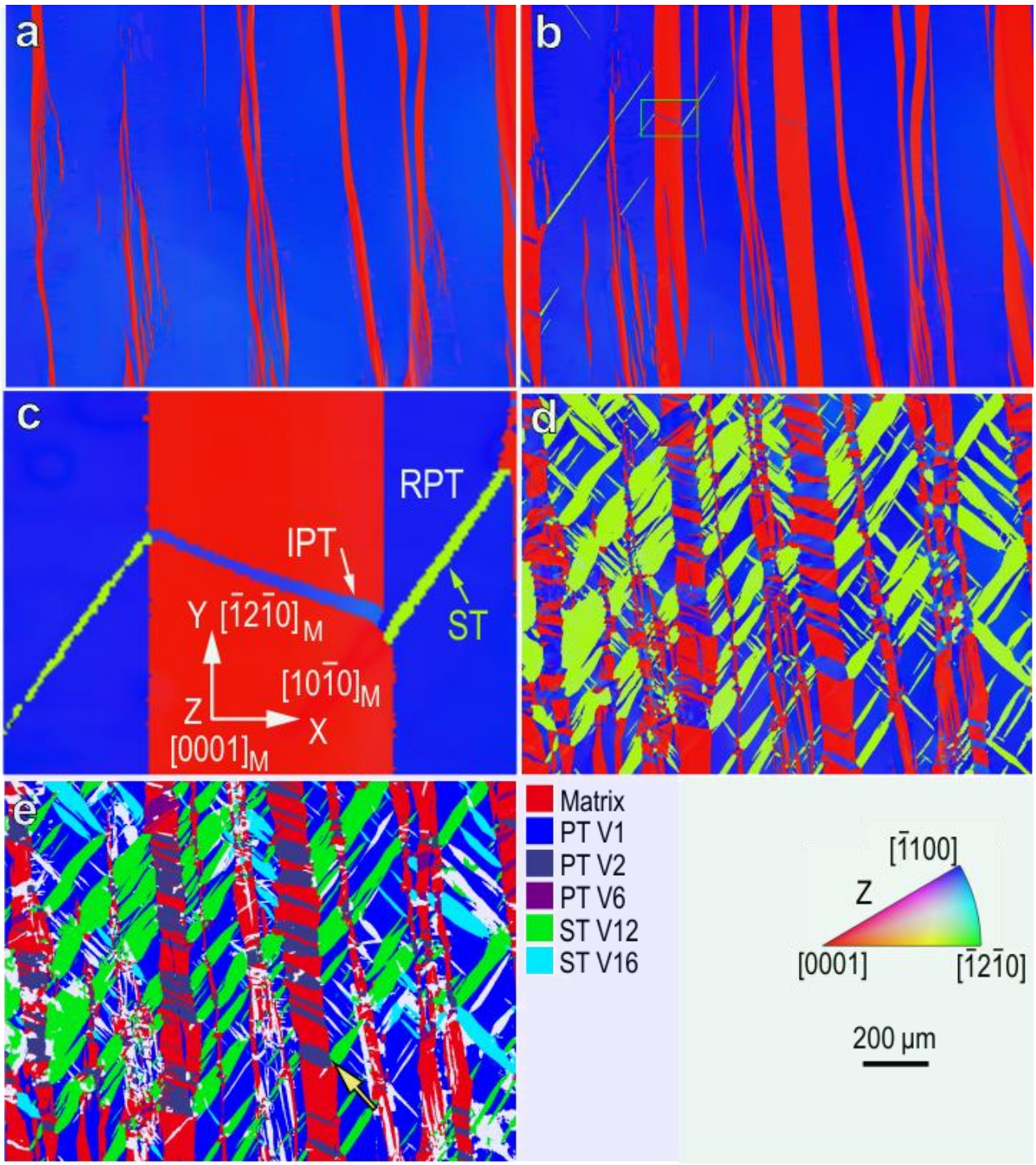

Fig. 5 Microstructure of a Mg single crystal first compressed along the *X* direction (approximately parallel to $[10\bar{1}0]$) with a magnitude of 0.075 (a), and then compressed along the *Y* direction (approximately parallel to $[\bar{1}2\bar{1}0]$) to a strain of 0.014 (b). A local region in (b) marked by the rectangular frame is enlarged in (c) where the IPT, RPT and an example of ST are marked. The $[10\bar{1}0]$, $[\bar{1}2\bar{1}0]$ and [0001] of the matrix are indexed and the subscript M means the matrix. After the compressive strain along the *Y* direction further increased to 0.035, the corresponding microstructure is shown in (d). (a) − (d) are coloured according to the inversed pole figure (IPF) of the direction perpendicular to the characterized surface, while in (e) the primary twin (PT) variants V1, V2 and V6, and the ST variants V12 and V16 are filled by different colours. All the other twin variants are shown in white. An example of V2−V12 pair is marked by a yellow arrow. The viewing direction is along [0001] of the matrix.

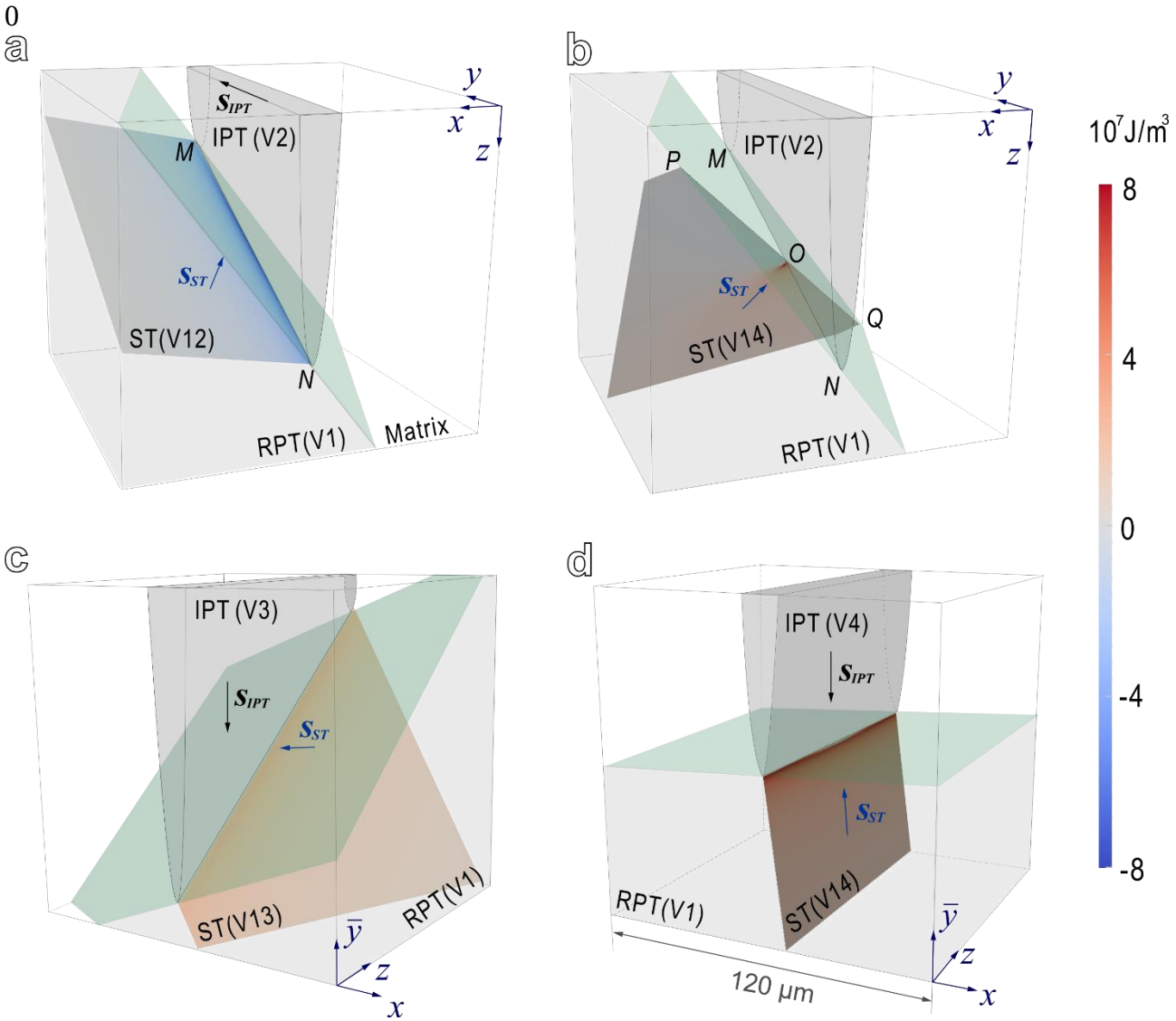

Fig. 6 Distribution of the interaction energy between IPT and ST on the twin plane of ST in the twin-twin intersection region of IPT and RPT. The IPT, RPT and ST variants are V2, V1 and V12 in (a); V2, V1 and V14 in (b); V3, V1 and V13 in (c) and V4, V1, V14 in (d). Both IPT and RPT crystals are in grey colour and the twin plane of RPT is coloured in light green. Values of the interaction energy are represented by the scale bar on the right. $\boldsymbol{s}_{IPT}$ and $\boldsymbol{s}_{ST}$ are twin shear directions of IPT and ST respectively.

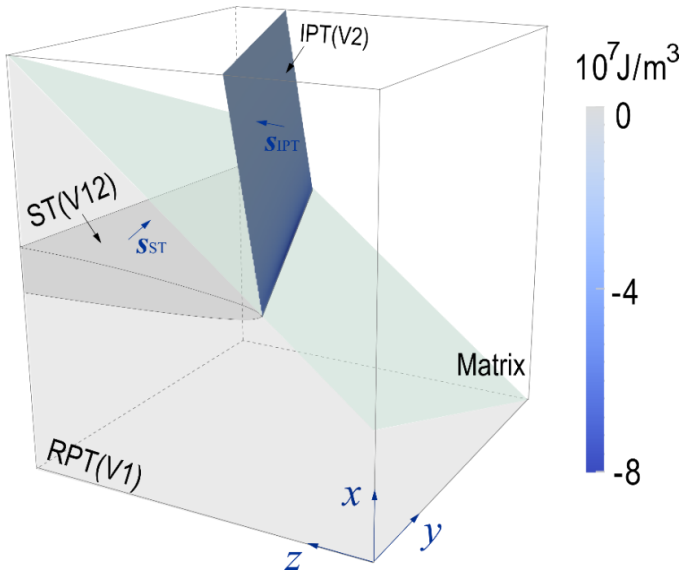

Fig. 7 Distribution of the interaction energy between ST and IPT (the situation that ST triggers IPT) on the twin plane of the to-be-nucleated IPT. The IPT, RPT and ST variants are V2, V1 and V12. Both pre-existing ST and RPT crystals are in grey colour and the twin plane of RPT is coloured in light green. Values of the interaction energy are represented by the scale bar on the right. $\boldsymbol{s}_{IPT}$ and $\boldsymbol{s}_{ST}$ are twin shear directions of IPT and ST, respectively.

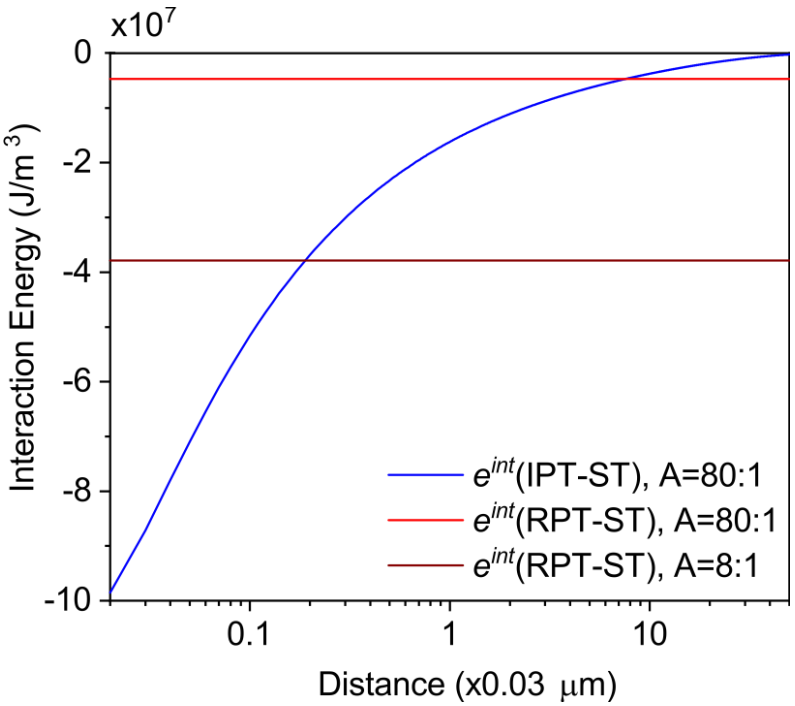

Fig. 8 Comparison of the values of interaction energy between the stress field of IPT and SFTS of ST (blue line), e^{int}(IPT– ST), and that between the back-stress of RPT and SFTS of ST (red and maroon lines), e^{int}(RPT– ST), varying as a function of the distance to the intersection line between the twin planes of IPT and ST. The aspect ratio of IPT is 80:1, while that of RPT is 80:1 (red line) and 8:1 (maroon line).

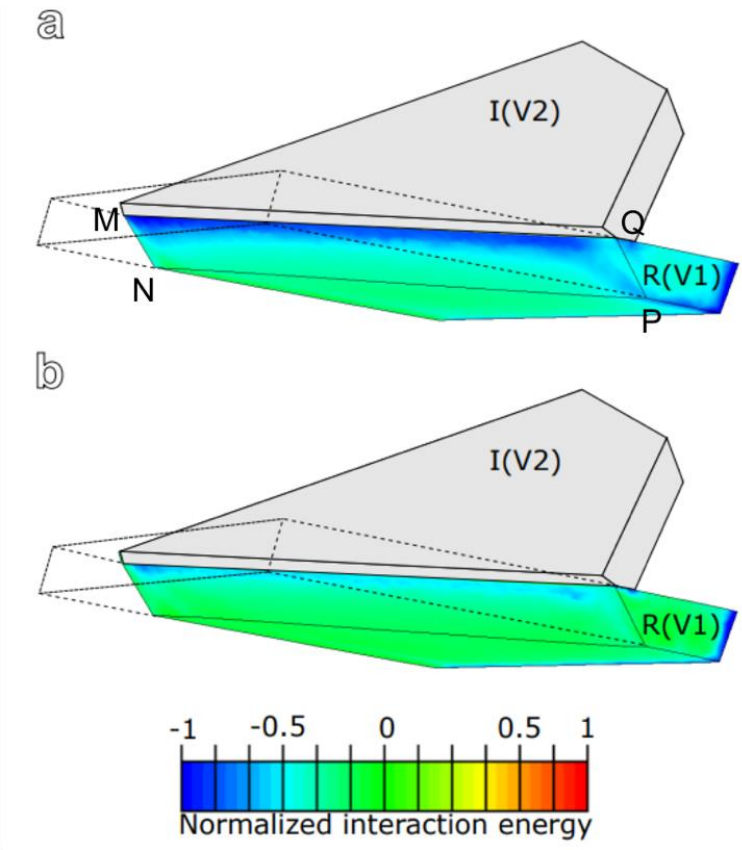

Fig. 9 Three-dimensional full field finite element (FE) calculations of the interaction energy between IPT (V2) and ST (V12) without (a) and with (b) considering effects of basal slip. The calculated interaction energies are normalised, i.e., if only considering the elastic strain energy, the minimum interaction energy value is set to –1. The calculation results are viewed on the twin plane of V12, which is plane MNPQ in (a).

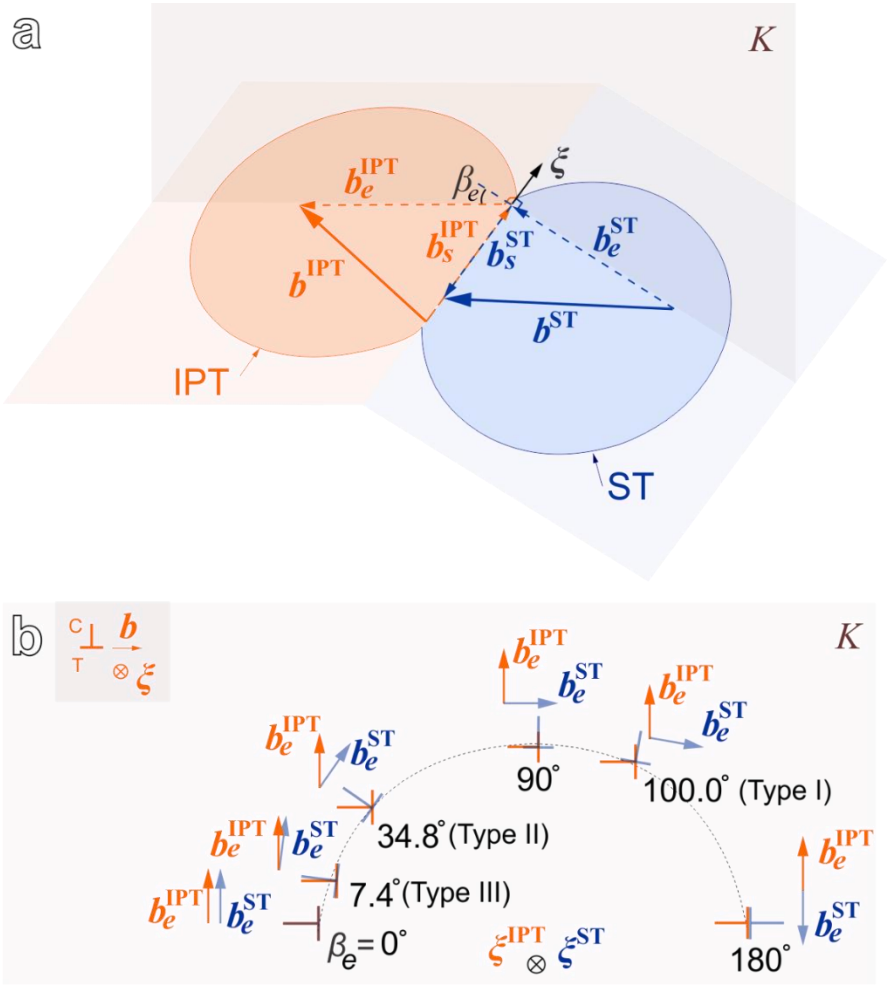

Fig. 10 (a) Schematic diagram showing two twinning dislocations, one on the twin plane of IPT and the other on the twin plane of ST intersecting the IPT twin plane. The Burgers vectors of these two twining dislocations are $\boldsymbol{b}^{IPT}$ and $\boldsymbol{b}^{ST}$. Each of them can be decomposed to an edge ($\boldsymbol{b}_e^{IPT}$, $\boldsymbol{b}_e^{ST}$) and a screw ($\boldsymbol{b}_s^{IPT}$, $\boldsymbol{b}_s^{ST}$) component. The angle between $\boldsymbol{b}_e^{IPT}$ and $\boldsymbol{b}_e^{IPT}$ is marked by β_e. At the intersection line between the twin planes of IPT and ST, the two twinning dislocations are parallel to each other, and the sense vector of these two dislocations are set parallel, marked by $\boldsymbol{\xi}$. The plane K is defined by the cross product of $\boldsymbol{b}_e^{IPT}$ and $\boldsymbol{b}_e^{IPT}$. (b) In plane K, variation of the interaction of the edge components of these two twining dislocations varies as a function of the angle β_e. The sense vectors of these two twinning dislocations, $\boldsymbol{\xi}^{IPT}$ and $\boldsymbol{\xi}^{ST}$, are perpendicular to K and pointed towards the viewing plane. The tension and compression strain regions around a single edge dislocation line are marked by T and C, respectively.

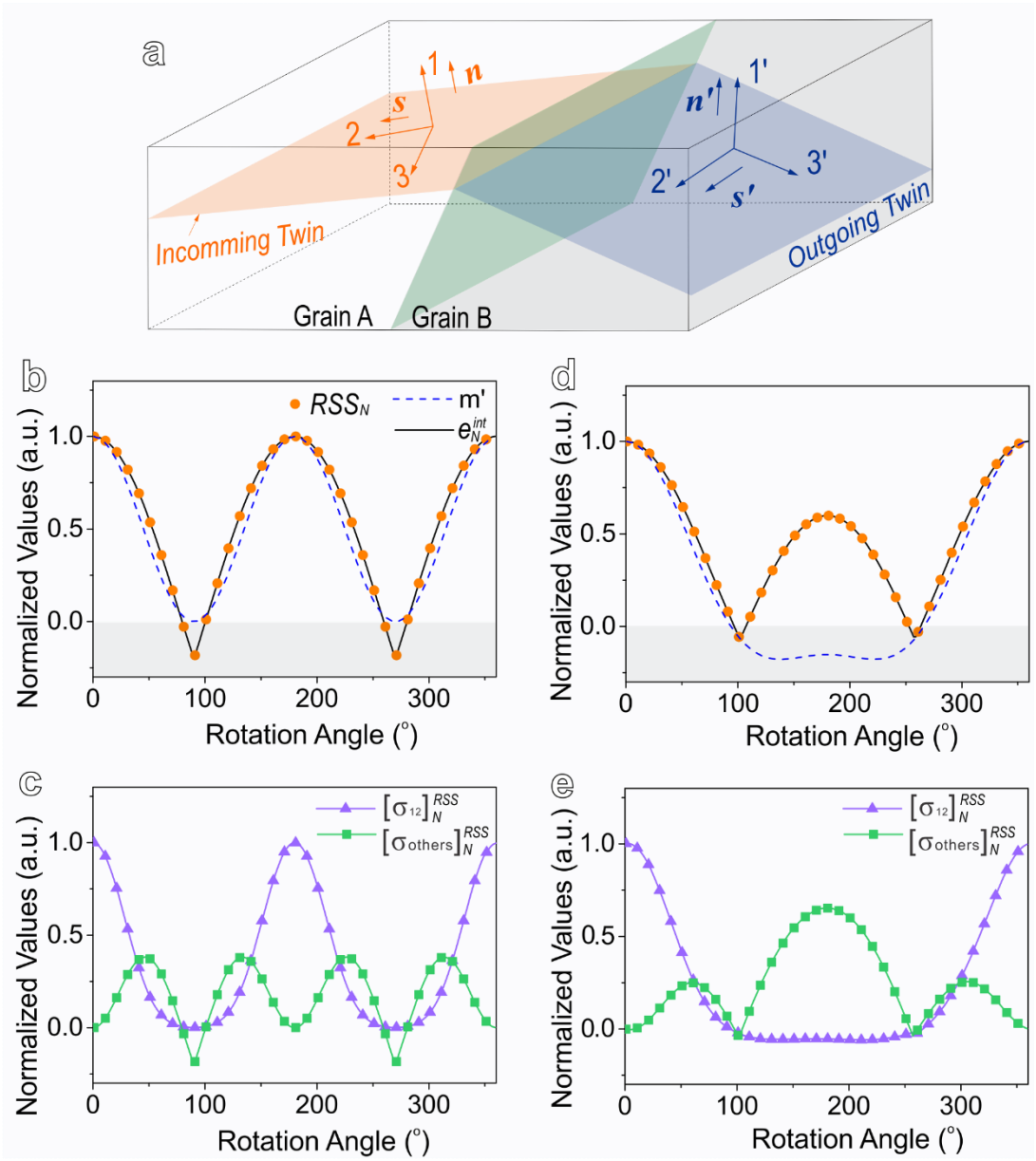

Fig. 11 Comparison of the application ranges of the compatibility factor m', the normalised resolved shear stress, σ_N^{RSS}, and the normalised interaction energy, e_N^{int} for twin transmission. (a) Schematic diagram showing the positions of an incoming twin and an outgoing twin in two neighbouring grains *A* and *B*. Two cases with typical rotation axes are compared: (b)–(c) rotation around $[2\bar{1}\bar{1}0]$ of grain *A*, and (d)–(e) rotation around $[10\bar{1}2]$ of grain *A*. The values of σ_N^{RSS}, e_N^{int} and m' are compared in (b) and (d). The contributions of σ_{12} (purple line) and other stress components (e.g. σ_{11}, σ_{22}, σ_{33}, σ_{13}, σ_{23}) (green line) to RSS of the outgoing twin are compared in (c) and (e).

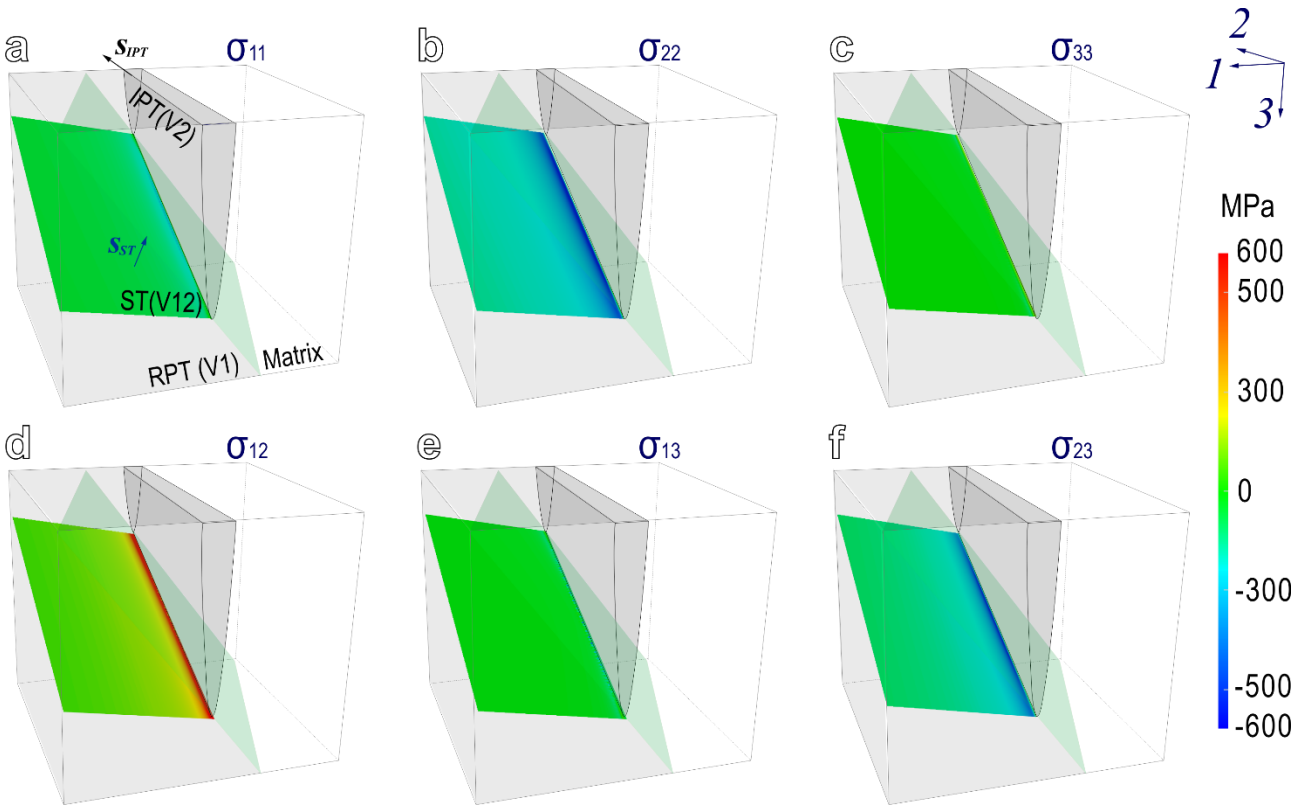

Fig. 12 Distribution of the stress field generated by IPT(V2) on the twin plane of ST (V12) at the twin-twin intersection region: (a) σ_{11}, (b) σ_{22}, (c) σ_{33}, (d) σ_{12}, (e) σ_{13}, and (f) σ_{23}. Both IPT and RPT are coloured in grey and the twin plane of RPT is coloured in green. Values of the stress components are represented by the scale bar on the right. The stress components are defined in the *123* coordinate system, where *1* and *2* directions are the twin plane normal and the twin shear directions of the IPT, respectively.

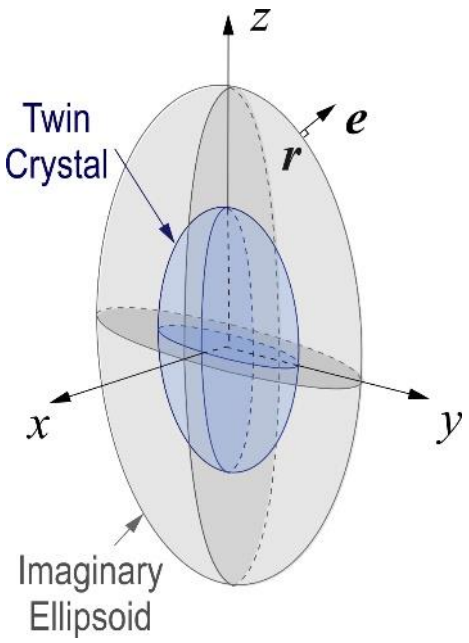

Fig. A1 Schematic diagram of an oblate spheroid twin crystal (in blue). For each arbitrary point r outside the twin crystal, an imaginary ellipsoid (in grey colour) is constructed and the corresponding outward unit normal vector is denoted by $\boldsymbol{e}$.

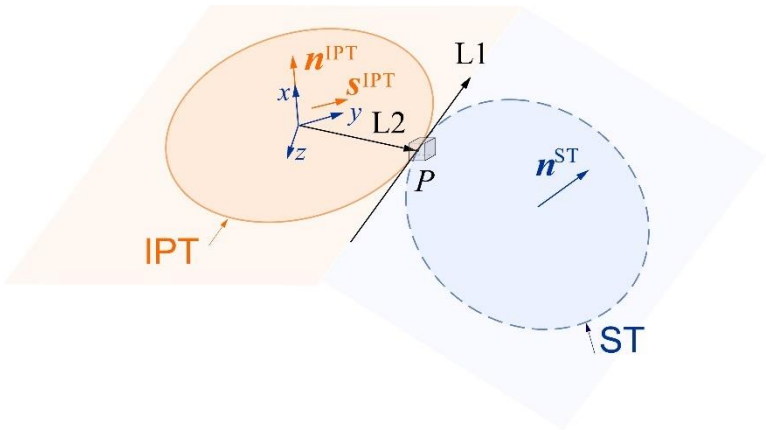

Fig. A2 Schematic diagram showing the calculation of interaction energy between the stress field of the twin tip of the IPT and the SFTS of the to-be-nucleated ST. The calculation is operated in the *xyz* coordinate system where $x//\boldsymbol{n}^{\mathbf{IPT}}$, $y//\boldsymbol{s}^{\mathbf{IPT}}$, and $z//(\boldsymbol{n}^{\mathbf{IPT}} \times \boldsymbol{s}^{\mathbf{IPT}})$, where $\boldsymbol{n}^{\mathbf{IPT}}$ and $\boldsymbol{s}^{\mathbf{IPT}}$represent the twin plane normal and twin shear directions of IPT. Interaction energy distribution in a cubic region around the contact point *P*.

Tables

Table 1 Twinning systems and schematic plot showing the orientations of the six primary $\{10\bar{1}2\}$ twin variants, V*i* (*i* = 1– 6). Orientations of the secondary twin variants formed in the primary twin variant V1, V1*j* (*j* = 1–6), are represented by a (0002) pole figure.

Primary Twin Variants	Twinning Systems	Schematic Orientatons	(0002) Pole Figure
V1	$(10\bar{1}2)[\bar{1}011]$	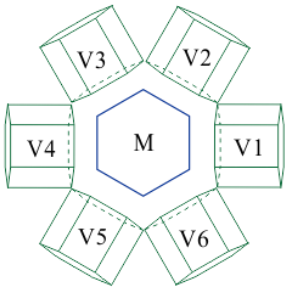	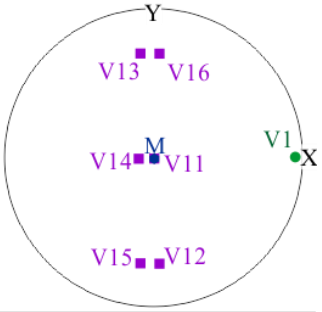
V2	$(01\bar{1}2)[0\bar{1}11]$		
V3	$(\bar{1}102)[1\bar{1}01]$		
V4	$(\bar{1}012)[10\bar{1}1]$		
V5	$(0\bar{1}12)[01\bar{1}1]$		
V6	$(1\bar{1}02)[\bar{1}101]$		

Table 2 The twin shear direction $\mathbf{s}/\gamma^0$, twin plane normal **n** and SFTS $\boldsymbol{\varepsilon}$ of primary twin V1 and secondary twin V1*j* (*j* = 1–6) expressed in the *XYZ* coordinate system, where *X*//$[10\bar{1}0]$, *Y*//$[\bar{1}2\bar{1}0]$, and *Z*//[0001] of the matrix.

PT	$\boldsymbol{s^1}/\gamma^0$	$\boldsymbol{n^1}$	**SFTS**($\boldsymbol{\varepsilon^1}$)
V1	$\begin{pmatrix}-0.7297\\0\\0.6838\end{pmatrix}$	$\begin{pmatrix}0.6838\\0\\0.7297\end{pmatrix}$	$\begin{pmatrix}-0.0649 & 0 & -0.0043\\0 & 0 & 0\\-0.0043 & 0 & 0.0649\end{pmatrix}$
ST	$\boldsymbol{s^{1j}}/\gamma^0$	$\boldsymbol{n^{1j}}$	**SFTS(** $\boldsymbol{\varepsilon^{1j}}$ **)**
V11	$\begin{pmatrix}-0.7297\\0\\0.6838\end{pmatrix}$	$\begin{pmatrix}-0.6838\\0\\-0.7297\end{pmatrix}$	$\begin{pmatrix}0.0649 & 0 & 0.0043\\0 & 0 & 0\\0.0043 & 0 & -0.0649\end{pmatrix}$
V12	$\begin{pmatrix}0.7060\\0.6319\\-0.3197\end{pmatrix}$	$\begin{pmatrix}0.7060\\-0.5922\\0.3885\end{pmatrix}$	$\begin{pmatrix}0.0648 & 0.0018 & 0.0032\\0.0018 & -0.0487 & 0.0282\\0.0032 & 0.0282 & -0.0162\end{pmatrix}$
V13	$\begin{pmatrix}0.6587\\0.6319\\0.4084\end{pmatrix}$	$\begin{pmatrix}0.7503\\-0.5922\\-0.2938\end{pmatrix}$	$\begin{pmatrix}0.0643 & 0.0055 & 0.0073\\0.0055 & -0.0487 & -0.0278\\0.0073 & -0.0278 & -0.0156\end{pmatrix}$
V14	$\begin{pmatrix}0.6350\\0\\0.7725\end{pmatrix}$	$\begin{pmatrix}0.7725\\0\\-0.6350\end{pmatrix}$	$\begin{pmatrix}0.0638 & 0 & 0.0126\\0 & 0 & 0\\0.0126 & 0 & -0.0638\end{pmatrix}$
V15	$\begin{pmatrix}0.6587\\-0.6319\\0.4084\end{pmatrix}$	$\begin{pmatrix}0.7503\\0.5922\\-0.2938\end{pmatrix}$	$\begin{pmatrix}0.0643 & -0.0055 & 0.0073\\-0.0055 & -0.0487 & 0.0279\\0.0073 & 0.0279 & -0.0156\end{pmatrix}$
V16	$\begin{pmatrix}0.7060\\-0.6319\\-0.3197\end{pmatrix}$	$\begin{pmatrix}0.7060\\0.5922\\0.3885\end{pmatrix}$	$\begin{pmatrix}0.0648 & -0.0018 & 0.0032\\-0.0018 & -0.0487 & -0.0282\\0.0032 & -0.0282 & -0.0162\end{pmatrix}$

Table 3 Crystallographic features of the three IPT–RPT–ST configurations (i.e., Types I, II and III, examples of which are V2–V1–V12, V3–V1–V13 and V4–V1–V14, respectively), including the common intersection line among the twin planes of IPT, RPT, and ST; the misorientations between IPT and RPT, and between IPT and ST; the compatibility factor, *m′*, between IPT and ST; and the angle between the common intersection line and the twin shear directions of IPT/ST, i.e., α_{IPT}/α_{ST}.

Configuration	I	II	III
IPT–RPT–ST	V2–V1–V12	V3–V1–V13	V4–V1–V14
Intersection Line	$[4\bar{2}\bar{2}\bar{3}]$	$[\bar{2}201]$	$[1\bar{2}10]$
Misorientation IPT−RPT	$60.0^{o}\langle\overline{12}\ 12\ 0\ 1\rangle$	$60.4^{o}\langle\bar{7}\ 8\ \bar{1}\ 0\rangle$	$7.4^{o}\langle\bar{2}\ 1\ 1\ 0\rangle$
Misorientation IPT−ST	$49.6^{o}\langle\bar{9}\ 9\ 0\ 4\rangle$	$37.9^{o}\ \langle\bar{2}\ 2\ 0\ 1\rangle$	$78.9^{o}\langle\bar{1}\ 2\ \bar{1}\ 0\rangle$
m′ (IPT−ST)	−0.1525	−0.0988	−0.9832
α_{IPT}	24.84°	69.28°	90°
α_{ST}	24.84°	69.28°	90°

Table 4 Euler angles and Schmid factor *m* of the twin crystals, and the geometrical compatibility factor, *m′*, between the IPT–ST adjoining twin pairs in IPT–RPT–ST configurations in regions marked in Fig. 2.

Regions	Twins	Euler angle (°)			*m*	*m′*
1	RPT	113	101	32	0.47	
	IPT	51	98	24	0.48	–0.12
	ST	24	63	50	–0.09	
2	RPT	107	100	30	0.48	
	IPT	170	97	38	0.48	–0.15
	ST	19	120	49	–0.10	
3	RPT	173	96	41	0.48	
	IPT	110	103	31	0.46	–0.12
	ST	81	70	54	–0.05	
4	RPT	112	102	30	0.44	
	IPT	173	94	44	0.46	–0.12
	ST	31	64	46	–0.08	
5	RPT	53	92	20	0.48	
	IPT	174	99	40	0.47	–0.15
	ST	138	70	4	–0.05	

Table 5 Schmid factor m of the primary and secondary twin variants in the single crystal sample described in Section 3.3.

PT	**V1**	**V2**	**V3**	**V4**	**V5**	**V6**
m	0.01	0.43	0.30	0.01	0.43	0.30
ST		**V12**	**V13**	**V14**	**V15**	**V16**
m		0.36	0.36	-0.01	0.34	0.34

Table 6 List of all 30 IPT–RPT combinations, and the ST variants that can form Type I IPT–RPT–ST configuration.

IPT \ RPT	V1	V2	V3	V4	V5	V6
V1	N/A	Type I (ST V21)	Type II	Type III	Type II	Type I (ST V61)
V2	Type I (ST V12)	N/A	Type I (ST V32)	Type II	Type III	Type II
V3	Type II	Type I (ST V23)	N/A	Type I (ST V43)	Type II	Type III
V4	Type III	Type II	Type I (ST V34)	N/A	Type I (ST V54)	Type II
V5	Type II	Type III	Type II	Type I (ST V45)	N/A	Type I (ST V65)
V6	Type I (ST V16)	Type II	Type III	Type II	Type I (ST V56)	N/A

Table 7 Interaction energies between the back-stress of RPT/applied stress and SFTS of ST. The RPT is assumed to be V1, and its corresponding ST variants are V1j (j=2–6). Two types of applied stresses are considered: 100 MPa uniaxial tensile stress along [0001], $\sigma_{\mathrm{T}}^{\mathrm{app}}$, and 100 MPa compressive stress along $[\bar{1}2\bar{1}0]$ of the matrix, $\sigma_{\mathrm{C}}^{\mathrm{app}}$.

ST	**V12**	**V13**	**V14**	**V15**	**V16**
$e^{\mathrm{int}}(\mathrm{RPT—V1}j)$ (10^6 J/m^3)	−4.67	−4.64	−7.42	−4.64	−4.67
$e^{\mathrm{int}}(\sigma_{\mathrm{T}}^{\mathrm{app}}—\mathrm{V1}j)$ (10^6 J/m^3)	1.61	1.56	6.38	1.56	1.61
$e^{\mathrm{int}}(\sigma_{\mathrm{C}}^{\mathrm{app}}—\mathrm{V1}j)$ (10^6 J/m^3)	−4.68	−4.68	0.13	−4.42	−4.42

Table 8 Material parameters used in FE calculations.

Elastic constant	C_{11} (GPa)	C_{12} (GPa)	C_{13} (GPa)	C_{33} (GPa)	C_{44} (GPa)
	63.5	24.85	20	66	19.325
Basal slip	τ_{c0} (MPa)	Γ_0	n		
	3.3	0.006	0.01		